The Physico-Chemical Properties of a Subducted Slab from Garnet Zonation Patterns (Sesia Zone, Western Alps)

MATTHIAS KONRAD-SCHMOLKE[1]*, JOCHEN BABIST[1], MARK R. HANDY[1] AND PATRICK J. O'BRIEN[2]

[1]FREIE UNIVERSITÄT BERLIN, DEPARTMENT OF EARTH SCIENCES, MALTESERSTR. 74–100, 12249 BERLIN, GERMANY

[2]UNIVERSITY OF POTSDAM, DEPARTMENT OF GEOSCIENCES, KARL-LIEBKNECHT-STRASSE 24–25, 14476 GOLM, GERMANY

Garnets in continentally derived high-pressure (HP) rocks of the Sesia Zone (Western Alps) exhibit three different chemical zonation patterns, depending on sample locality. Comparison of observed garnet zonation patterns with thermodynamically modelled patterns shows that the different patterns are caused by differences in the water content of the subducted protoliths during prograde metamorphism. Zonation patterns of garnets in water-saturated host rocks show typical prograde chemical zonations with steadily increasing pyrope content and increasing XMg, together with bell-shaped spessartine patterns. In contrast, garnets in water-undersaturated rocks have more complex zonation patterns with a characteristic decrease in pyrope and XMg between core and inner rim. In some cases, garnets show an abrupt compositional change in core-to-rim profiles, possibly due to water-undersaturation prior to HP metamorphism. Garnets from both water-saturated and water-undersaturated rocks show signs of intervening growth interruptions and core resorption. This growth interruption results from bulk-rock depletion caused by fractional garnet crystallization. The water content during burial influences significantly the physical properties of the subducted rocks. Due to enhanced garnet crystallization, water-undersaturated rocks, i.e. those lacking a free fluid phase, become denser than their water-saturated equivalents, facilitating the subduction of continental material. Although water-bearing phases such as phengite and epidote are stable up to eclogite-facies conditions in these rocks, dehydration reactions during subduction are lacking in water-undersaturated rocks up to the transition to the eclogite facies, due to the thermodynamic stability of such hydrous phases at high P–T conditions. Our calculations show that garnet zonation patterns strongly depend on the mineral parageneses stable during garnet growth and that certain co-genetic mineral assemblages cause distinct garnet zonation patterns. This observation enables interpretation of complex garnet growth zonation patterns in terms of garnet-forming reactions and water content during HP metamorphism, as well determination of detailed P–T paths.

INTRODUCTION

Detailed pressure–temperature–time $(P–T–t)$ paths provide important information about the tectonic and mineralogical processes responsible for the rapid burial and exhumation of high-pressure (HP) rocks in subduction zones (Carswell & Zhang, 1999; Peacock & Wang, 1999; Liou *et al.*, 2000; Aoya *et al.*, 2003). In addition, the bulk chemical evolution, especially the volatile content of the buried rocks, plays an important role during subduction and exhumation processes, because it influences the physical properties of the downgoing slab. In the case of devolatilization reactions, volatiles have a significant influence on seismicity and melt generation in subduction zones (e.g. Peacock, 1993; Schmidt & Poli, 1998). Furthermore, subduction of hydrous phases stable under mantle conditions contributes to volatile recycling into the mantle

*Corresponding author. E-mail: mkonrad@geo.uni-potsdam.de

(Liou & Zhang, 1995; Scambelluri *et al.*, 1995; Kerrick & Connolly, 2001). Many factors complicate the extraction of information on *P*, *T* and chemical composition from HP rocks. These factors include disequilibrium reactions, such as fractional crystallization (c.f. Spear, 1988), presence of relict mineral parageneses, devolatilization during burial, and polyphase metamorphic retrogression during exhumation. Due to the limitations of quantifying these disequilibrium conditions by conventional thermodynamic calculations, the mineralogical processes, especially the prograde *P–T* trajectories of the subducted rocks, are often very crudely defined.

Better constrained *P–T* paths and insight into the physico-chemical evolution of ultra-high-pressure (UHP) and HP terranes can be derived by interpreting relict zonation patterns in prograde metamorphic minerals in the light of thermodynamic forward modelling that incorporates element and fluid fractionation during metamorphism. Garnet is best suited for these purposes because its composition is very sensitive to changes in *P* and *T*, but also because cation diffusion in garnet is sufficiently slow to preserve compositional differences within grains. Thus, garnet growth zonation patterns are often used to constrain the *P–T* path of their host rock (Spear & Selverstone, 1983; Spear *et al.*, 1990; Menard & Spear, 1993; Okudaira, 1996; Ayres & Vance, 1997; Enami, 1998; Cooke *et al.*, 2000; Escuder-Viruete *et al.*, 2000), to determine the duration of metamorphic events (Lasaga & Jiang, 1995; Ganguly *et al.*, 1996; Ganguly & Tirone, 1999; Perchuk *et al.*, 1999), and to gain insight into crystal growth and transport mechanisms in metamorphic rocks (Hollister, 1966; Loomis, 1982; Cygan & Lasaga, 1982; Chernoff & Carlson, 1997; O'Brien, 1999; Spear & Daniel, 2001; Konrad-Schmolke *et al.*, 2005). Many HP and UHP rocks contain garnet with a growth zonation pattern reflected in core-overgrowth differences, both in inclusion assemblage and in major- and trace-element composition (O'Brien, 1997; Arenas *et al.*, 1997; Zhang *et al.*, 1997; Compagnoni & Hirajima, 2001). These chemical differences are reflected in very complicated zonation patterns, but the origin of these differences, although important for the petrological and geochronological interpretation, is poorly understood. In this study, we investigate complex garnet zonation patterns from a large number of structurally characterized sample locations in order to gain insight into the prograde *P–T*-composition (PTX) evolution of HP rocks from the Sesia Zone (Western Alps). Our approach compares modelled garnet zonation patterns, obtained by the method of Gibbs energy minimization and the THERIAK algorithm (de Capitani & Brown, 1987), with patterns observed in natural samples. In our calculations, we consider fractional garnet crystallization, water fractionation as well as different mono- and polymetamorphic *P–T* paths.

The Sesia Zone (SEZ) is of particular interest because it is one of the largest bodies of continental crust that has been subducted to ~60–65 km depth. Recent work has shown that subduction of continental crust is a common process that might be responsible for element recycling within the mantle and accretion of lower crustal material to the overriding plate (e.g. Walsh & Hacker, 2004). The effects of a polymetamorphic history in subducted rocks can be especially well studied in the SEZ, because it underwent a rift-related high-temperature (HT) metamorphic imprint prior to its HP metamorphic evolution (e.g. Lardeaux & Spalla, 1991; Rebay & Spalla, 2001). This evolution strongly influenced the volatile content of the SEZ rocks prior to the Alpine HP metamorphism and had a significant influence on the physical properties of the subducted rocks.

GEOLOGICAL SETTING

The SEZ underwent HP metamorphism during the Cretaceous to Tertiary convergence of the Apulian and European continental plates (e.g. Compagnoni *et al.*, 1977; Dal Piaz *et al.*, 1978; Duchêne *et al.*, 1997; Rubatto *et al.*, 1999). It is now exposed in the internal part of the Western Alps (Fig. 1). Prior to collision, the SEZ was part of the distal continental margin of the Adriatic plate that was separated from the European continent by the Liguria-Piemont Ocean. During plate convergence and subduction of the oceanic lithosphere, the Sesia rocks were tectonically detached from the continental margin and subducted to depths of about 60 km. Subsequent multistage exhumation placed the SEZ in the uppermost part of the Tertiary nappe pile (Dal Piaz *et al.*, 1972; Paschier *et al.*, 1981). The SEZ is bounded in its footwall by ophiolitic relics of the Liguria-Piemont Ocean and in its hanging wall by lower crustal rocks of the Southern Alpine Ivrea Zone. The Ivrea rocks are only marginally overprinted by Alpine greenschist-facies metamorphism (Schmid *et al.*, 1989). Both contacts are marked by first-order mylonitic shear zones that accommodated normal faulting as well as strike-slip movement during the syn-convergent exhumation of the Sesia and Piemont rocks (Schmid *et al.*, 1987; Wheeler & Butler, 1993; Reddy *et al.*, 1999).

Lithotectonic subdivisions

Lithologies in the SEZ mainly comprise metapelitic, meta–calc–pelitic and metagranitoid rocks intercalated with smaller slices of metabasites and subordinate lenses of carbonate- and quartz-rich rocks. They can be divided into four units (Fig. 1):

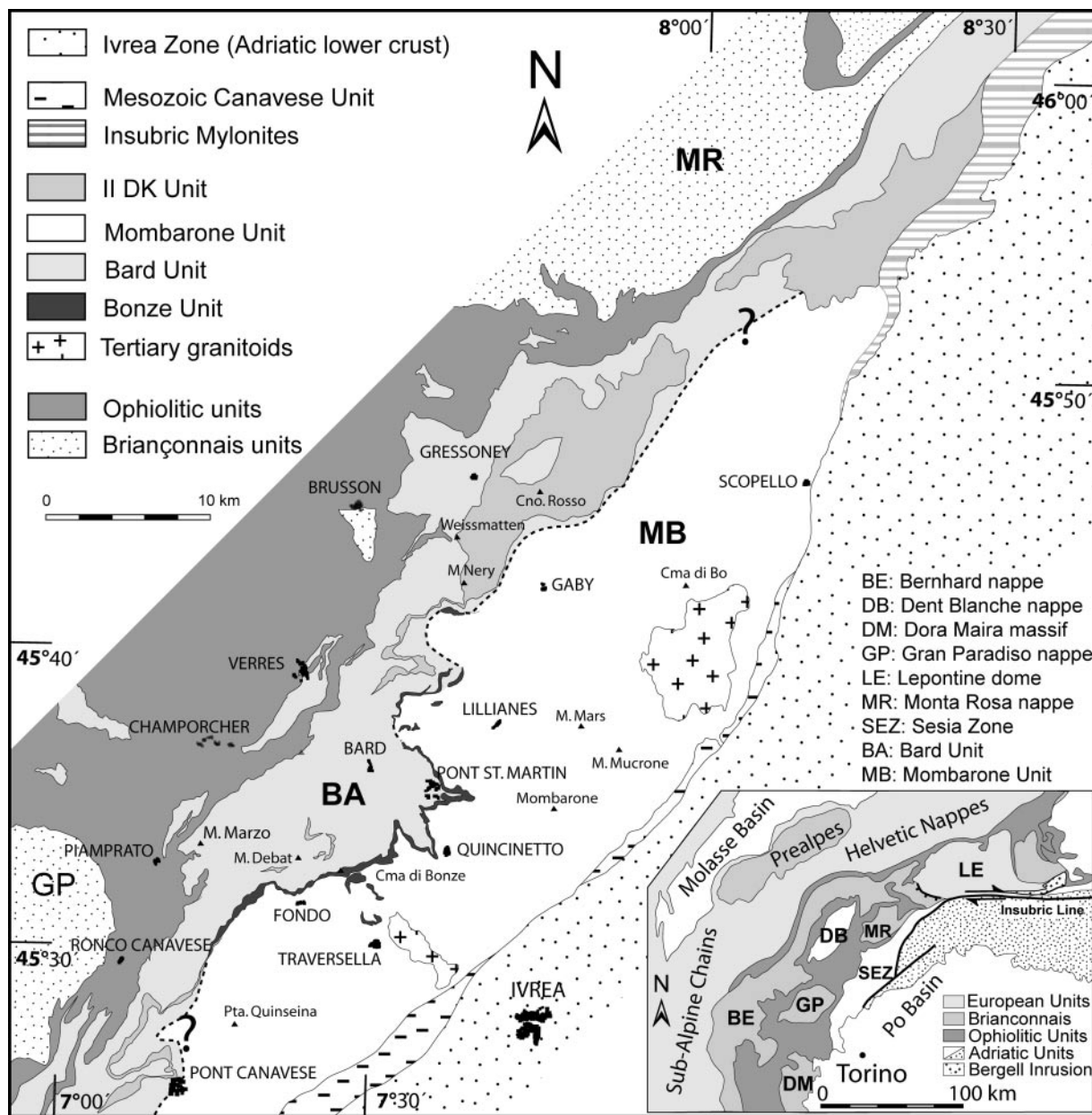(1) The *Mombarone Unit* best preserves Alpine HP mineral assemblages. It consists of large amounts of

Fig. 1. Simplified geological map of the central Sesia Zone (SEZ). The inset shows the position of the SEZ in the Western Alpine nappe pile. The rocks of the Bonze Unit mark the position of the nappe contact between the Mombarone Unit (MB) in the hanging wall and the Bard Unit (BA) in the footwall. The nappe contact is unclear in the northern part of the SEZ. Map modified after Venturini (1995).

coarse, quartz-rich garnet–zoisite–omphacite–sodic amphibole–phengite gneiss and schist, basic eclogite and small lenses of omphacite-, phengite- and zoisite-bearing marble (Dal Piaz *et al.*, 1972; Compagnoni & Maffeo, 1973; Gosso, 1977). In areas with a pervasive greenschist facies overprint, such as in the northern part of the SEZ, metapelites are mostly retrogressed to epidote–biotite/chlorite–white mica schists, whereas metabasites are predominantly transformed to chlorite–albite–

epidote–amphibole gneiss. Peak metamorphic conditions during Alpine subduction are 500–600°C at 1·5–2·0 GPa (Dal Piaz *et al.* 1972; Compagnoni & Maffeo 1973; Reinsch, 1979; Desmons & O'Neil, 1978; Compagnoni *et al.*, 1977; Oberhänsli *et al.*, 1985; Koons, 1986; Vuichard & Ballévre, 1988; Tropper *et al.*, 1999; Zucali *et al.*, 2002). Relics of pre-Alpine HT minerals, abundant in other units of the SEZ, are scarce in the Mombarone Unit (Dal Piaz *et al.*, 1972; Williams & Compagnoni, 1983).

(2) The *Bard Unit* forms the structurally lower margin of the SEZ (Fig. 1). It is characterized by a strong Alpine greenschist-facies overprint (Pognante *et al.*, 1987; Lattard, 1975; Compagnoni *et al.*, 1977; Stünitz, 1989) and consists mainly of fine-grained, biotite-bearing albite–white mica–epidote gneiss with minor intercalations of metabasic chlorite–calcic amphibole gneiss and subordinate phengite-bearing quartzites. Spalla *et al.* (1991) and Lardeaux and Spalla (1991) interpreted relics of omphacite found in the north-western part of the SEZ to reflect Alpine eclogite-facies metamorphism. Alpine peak metamorphic conditions were 400–500°C at 1·1–1·5 GPa (e.g. Lardeaux & Spalla, 1991). Previously, various authors have interpreted the contact with the Mombarone Unit to be a continuous metamorphic gradient ranging from eclogite-facies conditions in the Mombarone Unit to greenschist-facies conditions in the Bard Unit (e.g. Passchier *et al.*, 1981; Williams & Compagnoni, 1983). However, we found that the primary nappe contact is overprinted by a large sub-vertical mylonitic shear zone, suggesting tectonic juxtaposition of the Mombarone and Bard Units (Babist *et al.*, in press).

(3) The *Bonze Unit*, first described by Venturini *et al.* (1994; their MCC Unit), forms a band of Mesozoic, MORB-like metabasic rocks associated with smaller gabbroic lenses, manganese-rich quartzites and mica-bearing metacarbonate rocks. This unit can be mapped several tens of kilometres along strike. Peak metamorphic conditions in these rocks are around 550°C at 1·5 GPa (Venturini, 1995). The pressure is somewhat lower than that found in the Mombarone Unit. This thin slice of rocks of possibly transitional oceanic-continental origin is interpreted to separate the Bard and Mombarone units that were juxtaposed during Late Cretaceous subduction (e.g. Venturini, 1995).

(4) The *II DK Unit*, interpreted to form the structurally highest member of the SEZ, consists of pre-Alpine granulite and amphibolite facies schist and gneiss (Carraro *et al.*, 1970; Dal Piaz *et al.*, 1971; Lardeaux *et al.*, 1982). Most authors deduce peak temperatures between 700 and 800°C and pressures between 0·5 and 1·0 GPa for the pre-Alpine metamorphism (Lardeaux *et al.*, 1982; Rebay & Spalla, 2001). Equilibration under blueschist-facies conditions occurred mainly along the tectonic contact with the Mombarone Unit (Gosso, 1977; Ridley, 1989; Avigad, 1996). Alpine greenschist-facies overprinting in the II DK Unit is strongly dependent on deformation and affected mainly the smaller lenses of the II DK Unit in the central and southern part of the SEZ as well as the structurally higher parts of the large II DK bodies (e.g. Compagnoni *et al.*, 1977).

Structural framework

The Bard, Mombarone and II DK units developed into nappes during initial accretion in late-Cretaceous time (Babist *et al.*, in press). This interpretation is based mainly on the difference between the peak metamorphic conditions, as well as on the occurrence of Mesozoic sediments marking the nappe contacts. Structural analysis of the entire SEZ shows that the Mombarone Unit forms a weakly deformed, moderately NE-dipping core-like structure that is bounded towards the NW by a steeply dipping blueschist-facies transpressive shear zone. This shear zone effected initial exhumation of the Mombarone Unit from mantle depths (60 km) to 30–40 km in the middle crust (Babist *et al.*, in press). Mineral lineations and shear-sense indicators show an oblique exhumation of the southern Mombarone Unit with respect to the more external parts of the SEZ. Ridley (1989) and Avigad (1996) estimated 500–600°C at 0·9–1·4 GPa for this blueschist-facies deformation. This steeply dipping shear zone often, but not always, overprints the Bonze Unit.

Moderately dipping greenschist-facies top-down-to-E(SE) shear zones mark a vertically increasing strain gradient in the roof of the Mombarone unit and overprint the HP rocks as well as the blueschist-facies shear zone described above (Babist *et al.*, in press). The structural contact between the Sesia and Ivrea Zone is marked by later brittle and ductile deformation associated with the latest stages of the exhumation along steeply dipping backthrusts (e.g. Schmid *et al.*, 1987). Within the Bard Unit, the contact with the underlying Liguria-Piemont ophiolites is marked by a top-down-to-SE, mylonitic normal fault, which was active under retrograde greenschist-facies conditions. This fault is interpreted to be associated with the exhumation of Tertiary eclogite facies oceanic remnants within the Liguria-Piemont Unit (Wheeler & Butler, 1993; Reddy *et al.*, 1999).

RESULTS
Sample locations and garnet zonation patterns

Garnets are widely distributed in the II DK, the Bonze and the Mombarone Units. We sampled all three units. This sampling revealed a large variety of garnet zonation patterns that correspond with the tectonic units. Most of these zonation patterns show a significant difference between core and rim composition, although the transition from core to rim is smooth in some samples and
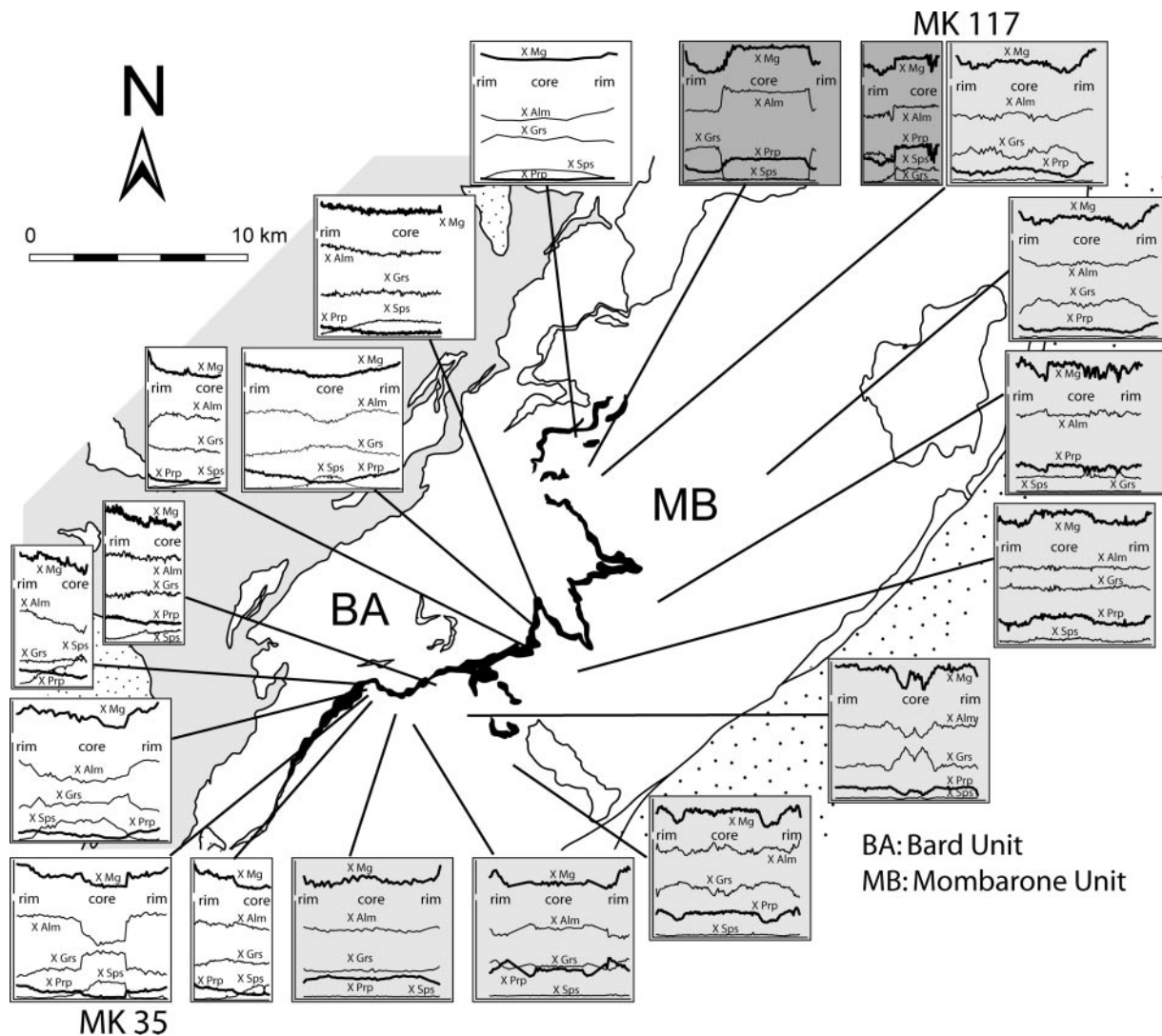
Fig. 2. Sample locations and garnet compositional profiles from the central Sesia Zone. Sample locations of group I garnets (white-background profiles) are mainly restricted to the nappe contact between the Mombarone and Bard Units as well as to the Bonze Unit. Group II (dark-grey background) and group III (light-grey background) garnets can only be found in samples from further within the Mombarone Unit. BA, Bard Unit; MB, Mombarone Unit.

step-like in others. The zonation patterns can be divided into three different groups, independent of host-rock lithology, but dependent on location (Fig. 2; see electronic supplementary material for detailed garnet compositional profiles and chemical bulk-rock compositions of the samples):

(1) A first group (white-background profiles in Fig. 2) is characterized by increasing pyrope content and increasing XMg (Mg/Mg + Fe) from core to rim. Although in a few cases, step-like zonation patterns with slightly decreasing Mg-content in parts of the zonation pattern occur, group I garnets generally show zonation patterns typical for prograde garnet growth in medium- to high-P rocks. Almandine (Fe/[Fe + Mg + Ca + Mn]) increases from core to inner rim, and then decreases towards the outer rim. Grossular decreases from core to rim or, in some samples, remains constant throughout the entire profile. Spessartine always has a bell-shaped profile, with mole fractions between 0·2 and 0·5 in the cores.

(2) The second group (dark-grey background profiles in Fig. 2) shows a characteristic step-like zonation pattern. The cores of group II garnets have a constant, in some samples slightly zoned almandine-rich, grossular-poor composition. The rims consist of almandine–grossular-rich garnet. At the transition

between core and rim, garnet composition changes drastically with respect to all major elements. Pyrope content and XMg decrease, then increase towards the outer rim. This drastic change in core-to-rim major element composition is in contrast to the trend in the core-to-rim transition in group I garnets.

(3) The zonation patterns of the third group (light-grey background profiles in Fig. 2), although slightly variable in shape and absolute composition, have apparent similarities. They always show a significant decrease in pyrope content and XMg over large parts of the profile at the transition between core and rim, but in contrast to group II garnets, the grossular-poor core and the abrupt compositional change between core and rim is lacking. Further, group III garnets have extremely low spessartine content and, in most samples, all components show complex zonation patterns. In some localities, garnets from group II and group III occur within the same sample.

Spatial distribution of the different zonation patterns

Interestingly, there is a spatial relationship between sample locality and garnet zonation pattern. Group I garnets occur in rocks sampled in the vicinity of the nappe contact between the Mombarone and Bard Units as well as in rocks from the Bonze Unit (Fig. 2). Although the composition of group I garnets changes slightly from sample to sample, depending on lithology, the shape of the zonation patterns (characteristic for group I) is generally identical. In contrast, samples from within the Mombarone Unit contain group II and III garnets. Samples that only contain garnets of group III are restricted to the internal parts of the Mombarone Unit. In this section, we describe three representative zonation patterns from two samples. The first contains garnets of group I, the second of groups II and III.

Sample MK 35 (group I garnets)

Sample MK 35 is a strongly foliated, quartz-rich meta-tonalitic rock (see Appendix Table 1 for the chemical analysis of the sample) from the contact zone between the Mombarone and Bard Units (Fig. 2). The Alpine HP mineral assemblage in this sample is strongly affected by a retrograde greenschist-facies overprint, resulting in the disequilibrium mineral assemblage biotite–chlorite–garnet–calcic amphibole–sodic amphibole–albite–epidote–phengite–quartz. Although relics of omphacite can be found in this sample, it is mostly retrogressed to white mica, albite, calcic amphibole and minor chlorite. Sodic amphibole is either completely altered or is replaced at its rim by biotite, chlorite and calcic amphibole. Garnets form clasts in the well developed

mylonitic foliation and range from small fragments to hypidiomorphic grains (up to 1·5 mm in diameter). Epidote and quartz are the most common inclusion phases in the cores of group I garnets, whereas inclusions in the rims, typically located in concentric inclusion zones, comprise epidote, rutile and quartz (Fig. 3a). Large (>0·5 mm) grains are very often atoll-like in shape with resorbed cores, entirely replaced by phengitic mica, epidote and/or quartz (Fig. 3a). Most group I garnets, as shown in the back-scattered electron (BSE) image in Fig. 3a, have a darker, irregularly formed core that is overgrown by a lighter inner rim and a darker outer rim. Newly formed garnet with the same composition as the brighter mantle region can be found within the resorbed cores (arrow in Fig. 3a). Figure 3b shows a group I garnet from this sample with a euhedral core that is only weakly affected by resorption (arrow). The white line represents the position of the compositional core-to-rim profile in Fig. 3c. This profile shows a step-like zonation pattern with an almandine–grossular-rich core and an almandine-rich mantle and rim. Apart from a small region between core and mantle, pyrope as well as XMg increase gradually. Spessartine shows a typical bell-shaped zonation with mole fraction values around 0·2 in the core and a slight irregular increase at the core-rim transition. The grossular content changes from between 0·35 to 0·4 in the core to values around 0·3 at the inner rim, decreasing to about 0·2 at the outer rim. Almandine content increases from 0·45 in the core to 0·8 at the inner rim, followed by a slight decrease to 0·7 near the outer rim.

Sample MK 117 (group II and III garnets)

Sample MK 117 is a quartz-rich zoisite–garnet–sodic amphibole–calcic amphibole–phengite gneiss with a strong foliation, defined by white mica and amphibole (see Appendix Table 1 for bulk rock chemistry). The foliation in this sample is parallel to that in the mylonitic shear zone that overprints the nappe contacts, but the sample is from further within the Mombarone Unit than MK35 (Fig. 2). Relict omphacitic pyroxene can be found in pseudomorphs consisting of albite, white mica, chlorite and calcic amphibole. Apart from the almost completely replaced omphacite, the HP assemblage is only partly replaced by greenschist-facies minerals. Retrogression is restricted to the grain edges of sodic amphibole, garnet and phengite. Garnets in this sample show a strongly bimodal grain size distribution and are typical for group II and III. Whereas group II garnets in this sample are between 1 and 5 mm in size and have irregular grain shapes, garnets of group III are smaller (up to 1 mm) and have subhedral to rounded and irregular shapes. Both types form clasts within the mylonitic foliation. Grain boundaries to other syn-metamorphic phases sometimes have reaction rims.
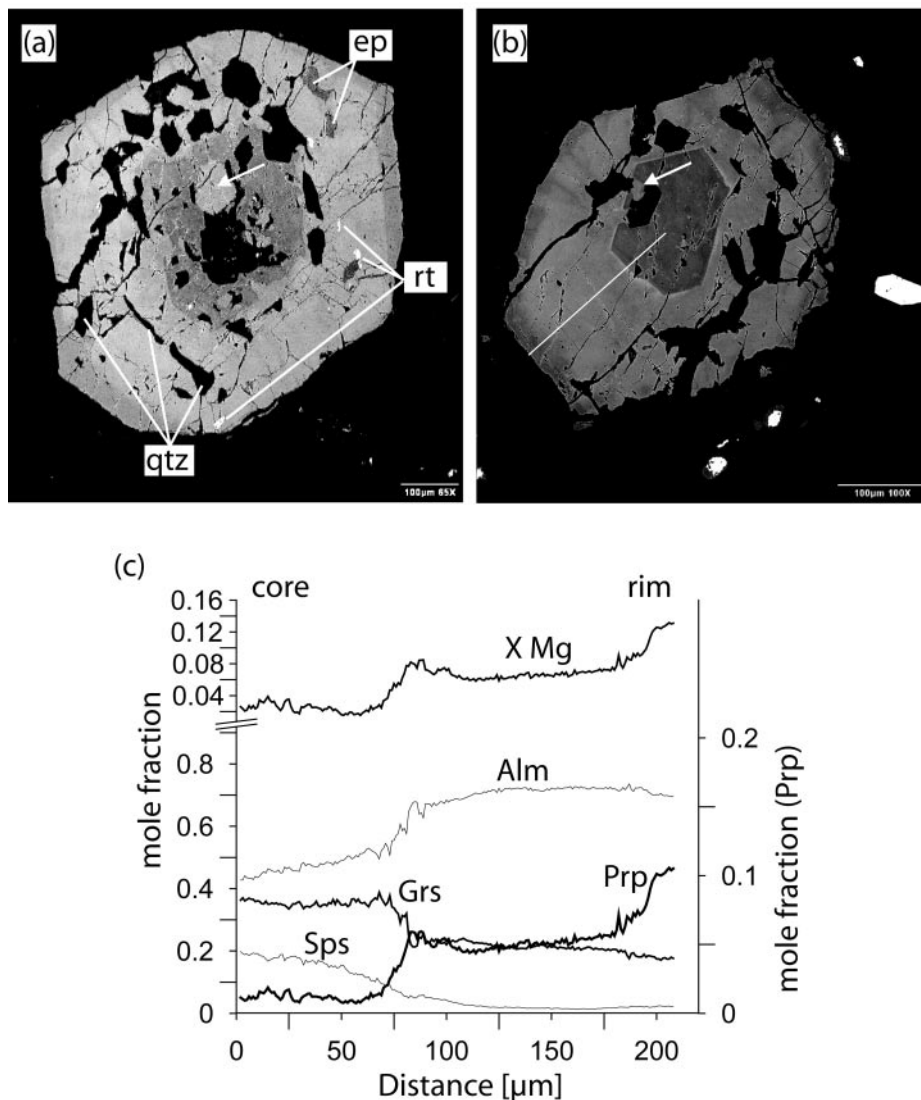
Group I garnets

Fig. 3. Group I garnets. (a) Back-scattered electron image of an atoll-like group I garnet from sample MK 35. The arrow marks new mantle material grown within the resorbed core. (b) Group I garnet with an almost unresorbed core from the same sample. Resorption is only indicated by small embayments filled with mantle material (arrow). (c) Compositional core–rim profile along the white line in (a).

Garnets of group II have inclusion-poor euhedral cores surrounded by inclusion-rich rims (Fig. 4a and b). The rims contain numerous epidote and rutile inclusions that are often concentrically arranged between core and inner rim. The BSE image in Fig. 4a shows a highly fractured group II garnet grain. Clearly visible is a bright core, overgrown by a darker rim. The image in Fig. 4b shows a closer view of the garnet overgrowth. The close-up image shows that the core is truncated by a dense network of cracks filled with garnet rim material. Associated with these cracks is a minor diffusional relaxation of the garnet core composition, as indicated by the darker areas around the filled cracks (Fig. 4b).

The darker rim has an inclusion-rich zone on the right side of the image (bright spots are rutile inclusions). Interestingly there is a small, irregularly shaped darker overgrowth followed by a brighter zone (arrow in Fig. 4b) that cannot be traced continuously around the core. Figure 4c shows a compositional core-to-rim profile across a large group II garnet (white line in Fig. 4a). The profile is characterized by a significant difference in core and rim composition. In the core, almandine content is constant between mole fractions of 0·71 and 0·75, pyrope and spessartine are between 0·1 and 0·16, and grossular is extremely low, between 0·01 and 0·05. Towards the rim, this composition
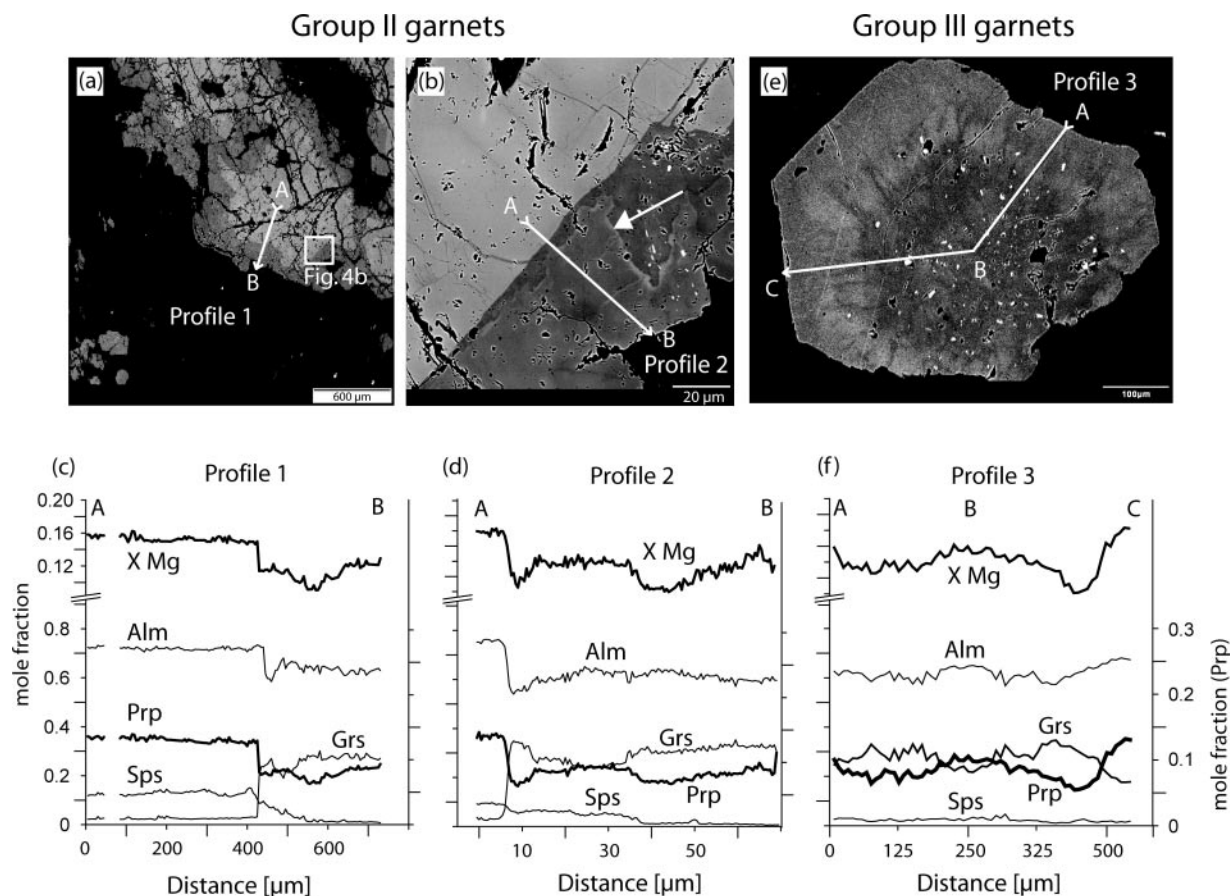
Fig. 4. Group II and III garnets. (a) Back-scattered electron (BSE) image of a large group II garnet with a light core that is overgrown by a darker irregularly shaped rim. The rectangle marks the close-up view in (b). (b) Detailed view of the overgrowth. Two different overgrowth zones are visible: a darker, irregularly shaped, sometimes inclusion-rich inner zone is overgrown by a thin light band (arrow), followed by a darker overgrowth. (c) Compositional profile of a typical group II garnet measured along the white line in (a). (d) Detailed compositional profile across the overgrowth in the group II garnet shown in (b). Note the complex zonation pattern in the darker overgrowth (profile 2). (e) BSE image of group III garnet from the same sample. The darker core shows numerous epidote, quartz and rutile inclusions. The lighter mantle and the rim are inclusion-poor or -free. (f) Compositional profile across the group III garnet in (e).

changes abruptly. Figure 4d displays a detailed compositional profile across the transition from core to rim. In the overgrowth, almandine drops to values around 0·6, then increases slightly again to 0·7, in some cases followed by a slight decrease to 0·65. Pyrope decreases at the core-overgrowth transition from 0·12 in the core to 0·08 in the innermost rim, decreases after a small plateau to values around 0·06, followed by a steady increase towards the outermost rim. The zonation pattern of grossular is also quite complex. At the core-rim transition grossular mole fraction rises to around 0·3 followed by an intermediate depression and a slight decrease towards the outer rim. Interestingly, there are two zones where the pyrope content shows small minima (Fig. 4d): first after the transition from core to rim, associated with an increase in grossular content, and second halfway towards the outer rim. Spessartine shows a slight increase at the core–rim transition (Fig. 4c) but

generally decreases from core to rim in two distinct plateau-like zones (Fig. 4d).

Group III garnets in this sample mostly occur as single grains in the matrix, but in few cases were found as inclusions in omphacite as well. They are mostly euhedral but sometimes show signs of resorption along the rims. They have numerous epidote and rutile inclusions concentrated in the core (Fig. 4e). Textural relations of matrix garnet suggest equilibrium paragen-eses with phengite and sodic amphibole. The profile in Fig. 4f shows the compositional variation along the white line in Fig. 4e. Although all investigated group III garnets in this sample are extremely Mn-poor, spessar-tine often preserves a zonation pattern, with slightly increasing Mn-content at the inner rim and towards the outermost rim (Fig. 4f). This may be the result of Mn back-diffusion due to garnet resorption. Almandine and grossular show the largest compositional variations and

most complex zonation patterns. Almandine decreases from mole fractions around 0·7 in the inner core to about 0·55 at the outer mantle and increases again to 0·7 at the outermost rim. The mole fraction of grossular shows the opposite pattern, increasing from core (0·2) to outer mantle (0·4) and decreasing to values below 0·2 at the outer rim. Both pyrope content and XMg show trends similar to that of almandine. They decrease from core to inner rim with a minimum at the transition between inner and outer rim and a strong increase towards the outer rim (Fig. 4f).

Comparison of observed zonation patterns with those derived from thermodynamic forward modelling

Forward modelling technique

The method of Gibbs energy minimization, utilizing internally consistent thermodynamic datasets and relevant activity–composition models, allows the determination of equilibrium mineral modes and compositions for a fixed bulk composition at any *P–T* condition (e.g. de Capitani & Brown, 1987; Connolly, 1995; Spear & Menard, 1989). In this study, we used the internally consistent dataset of Holland and Powell (1998) and various solid solution models. The solid solution models as well as a description of the model algorithm can be found in the Appendix.

Considering that a proportion of the volume of material in slow diffusing phases, such as garnet, is fractionated out of the effective (i.e. reacting) bulk-rock composition, we divided the *P–T* interval of interest into 100 regularly spaced *P–T* increments (Fig. 5), at each of which we calculate the thermodynamic properties of the chemical system. Modelling fractional crystallization involved modifying the chemical composition between two increments by removing the amount of each component incorporated in garnet from the bulk-rock composition, provided that garnet forms a stable phase in the assemblage. In contrast, in cases in which garnet resorption was assumed, fractionated material was returned to the reacting bulk-rock composition. With this gradually changing bulk-rock composition, it is possible to model the thermodynamic properties of the rock system affected by fractional crystallization of various minerals along the *P–T* path of interest. To model zonation patterns, we calculated the moles of garnet and its composition produced over the *P–T* interval between two increments. The amount of garnet is converted into a volume and a radial growth increment. Garnet composition is then plotted as a garnet zonation pattern by assuming a spherical grain shape. Further, we considered the effect of devolatilization by progressively removing free water from the system (cf. Konrad-Schmolke *et al.*, 2005) and the effect of
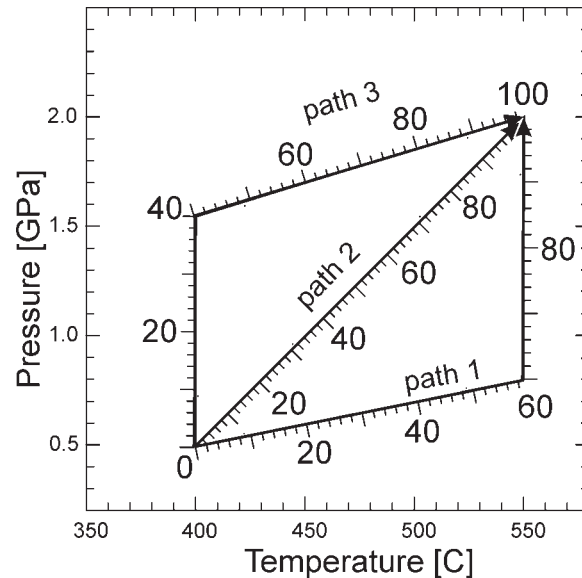

Fig. 5. *P–T* trajectories along which the metamorphic evolution of the samples is modelled. The *P–T* paths are divided into 100 increments (bold numbers) at each of which the thermodynamic properties are calculated based on the sample's effective bulk-rock composition.

water-undersaturation by defining the initial amount of hydrogen (and the proportional amount of oxygen) in the bulk-rock composition.

In order to gain insight into the processes leading to the different zonation patterns, and to reconstruct parts of the prograde metamorphic history of the eclogitic rocks in the Sesia Zone, we carried out thermodynamic forward modelling of garnet zonation patterns for the specific bulk-rock compositions of the samples (see Appendix) along three different *P–T*-paths starting at the same *P–T* conditions of 400°C at 0·5 GPa (Fig. 5):

(1) The first *P–T* path (path 1) leads into the epidote amphibolite facies, marked by rapidly increasing temperatures during the first part of the subduction path followed by a segment with little heating at increasing pressures.

(2) The second trajectory forms a straight line from 400°C at 0·5 GPa to 550°C at 2·0 GPa (path 2).

(3) The third path (path 3) reflects the situation in a fast subduction zone with rapidly increasing pressures at relatively low temperatures and increasing temperatures at greater depths.

(4) Additionally, we modelled a pre-Alpine HT path leading to peak conditions of 750°C at 0·8 GPa followed by a HP path.

To reconstruct the influence of varying water contents of the host-rock and water fractionation during metamorphism on the physico-chemical properties of the samples, we additionally modelled three different water
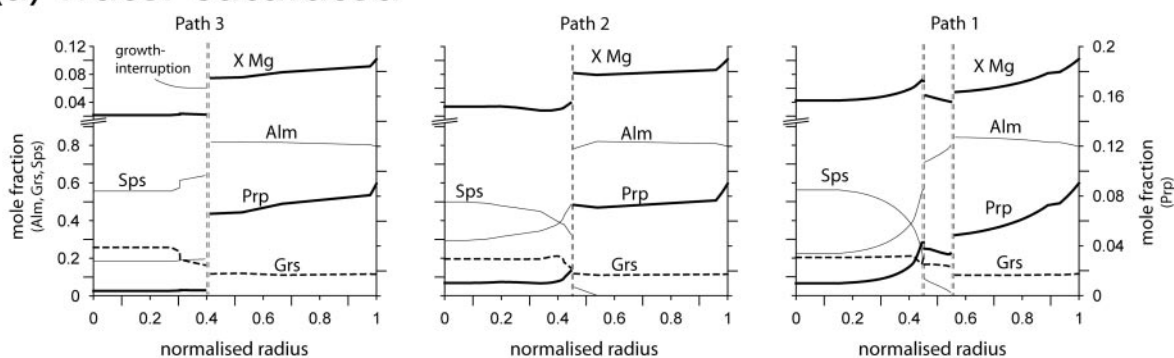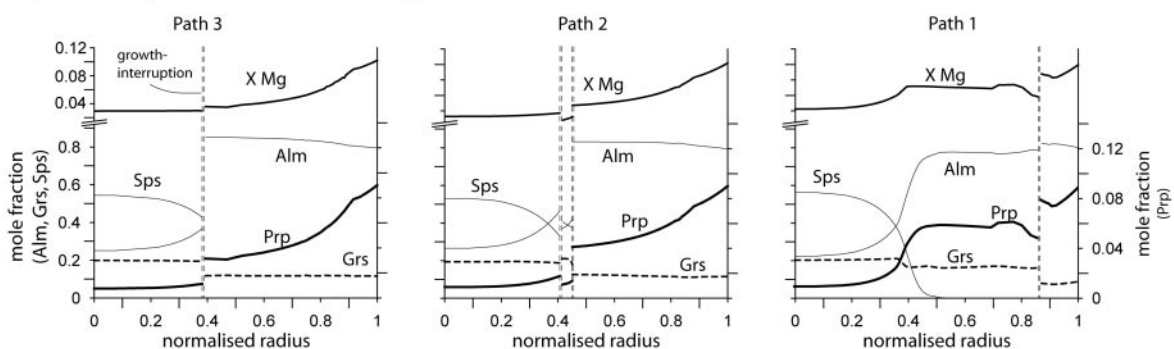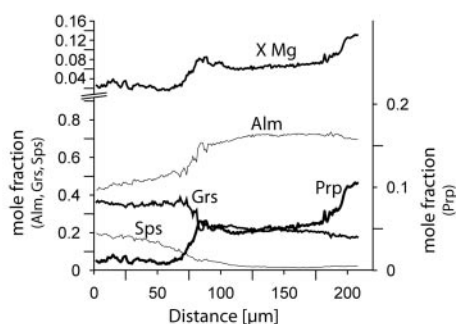
Fig. 6. Modelled garnet zonation patterns for sample MK 35 assuming a water-saturated (a) and a progressively dehydrated (b) host-rock along the three $P–T$ trajectories shown in Fig. 5. (a) The modelled pattern for path 2 closely resembles that of the natural sample (Fig. 6c) in the water-saturated model. (b) Modelled garnet zonation patterns for the same $P–T$ paths as in (a), but assuming dehydration during metamorphism. In this case, the naturally observed pattern is best reproduced by modelling along path 1. (c) Naturally observed core–rim profile of sample MK 35 for comparison.

fractionation scenarios for each of the above-mentioned $P–T$ trajectories:

(1) Water-saturated conditions; in this case, we calculated the thermodynamic parameters, assuming that water was always present as a free phase along the modelled $P–T$ path.

(2) Dehydration-only conditions; the rock is assumed to be initially water-saturated, but the amount of free water, if stable, is subtracted from the bulk composition at every calculated step.

(3) Water-undersaturated conditions; the rock initially contains less water than necessary to form a free fluid phase.

MK 35 (group I garnets)

Figure 6 shows the modelled garnet zonation patterns along the three different $P–T$ paths for water-saturated

(Fig. 6a) and dehydration-only (Fig. 6b) conditions. The different P–T trajectories as well as the different water fractionation conditions lead to significant differences in the garnet zonation patterns. Although in all cases, garnet growth occurs in at least two stages, indicated by the growth interruptions and the rapid compositional changes from core to rim, there are characteristic features that can be used to constrain the metamorphic evolution of the natural sample. Each diagram is characterized by distinct positions of the growth interruptions and the associated compositional changes.

The development of the garnet growth interruption along the P–T trajectory as well as the resulting changes in the modal amounts of minerals that affect garnet growth are displayed in Fig. 7. The modal abundance plot in Fig. 7a, as well as the pseudosections in Fig. 7c–f, are calculated along path 3, assuming progressive bulk-rock depletion due to water fractionation and fractional garnet crystallization (see Appendix Table 2 for calculated bulk rock compositions). The calculated zonation pattern is shown in Fig. 7b. Figure 7a shows that garnet grows in three stages, one of which occurs in the greenschist facies (between P–T increments 8 and 15), the second in the blueschist facies (between increments 60 and 95), and the third starts with the transition to the eclogite facies (at increment 95). The first garnet growth in the greenschist facies occurs at the expense of plagioclase and chlorite, indicated by the decreasing modal amounts of these phases in Fig. 7a. The resulting garnet composition is almandine- and spessartine-rich (Fig. 6b), typical for greenschist-facies garnets. Between the first and the second growth stages, there is a large P–T segment in which no new garnet material is produced (between increments 16 and 60; Fig. 7a).

The development of growth interruptions is nicely demonstrated by a sequence of pseudosections (Fig. 7c–f) calculated for those bulk-rock compositions that result from progressive depletion due to fractional crystallization and dehydration along the modelled P–T path. The diagrams are calculated for the bulk-rock compositions at the P–T increments labelled by the arrows in Fig. 7a. The first diagram (Fig. 7c) displays the phase relations and the modal amount of garnet (contours) for this sample, assuming water-saturated conditions and initial bulk-rock composition at the start of the forward modelling (first arrow in Fig. 7a). For simplicity, only those zero mode lines are shown that influence garnet growth. Mineral labels are marked on the 'present' side of the zero mode lines. The contours for the garnet mode indicate that garnet abundance is quite low up to temperatures between 450 and 550°C, depending on pressure, but increases rapidly at the transition to the eclogite and garnet–amphibolite facies. Interestingly, the stability field of garnet reaches well into the greenschist-facies P–T field between 1·0 and 1·3 GPa at 400°C.

The pseudosection in Fig. 7d is calculated for the bulk-rock composition at the onset of garnet growth (second arrow in Fig. 7a). Although the phase relations of most minerals are similar to those in the first diagram, the stability field of garnet is, due to water fractionation during the sample's prograde metamorphic evolution between 0·5 and 0·7 GPa, significantly enlarged at greenschist-facies conditions compared with the diagram in Fig. 7c. Due to the smaller water content, there is a P–T field above the zero mode line of H_2O, where the rock can become water-undersaturated with increasing pressure. The third diagram (Fig. 7e) is calculated for the bulk-rock composition at the last increment of the first garnet growth stage (arrow 3 in Fig. 7a). Due to fractional garnet crystallization, the stability field of garnet becomes smaller, and increasing pressure during metamorphism leads the sample out of the garnet stability field. The stable assemblage after the first garnet growth stage is feldspar (fsp) + sodic amphibole (gln) + calcic amphibole (amph) + epidote (ep) + quartz. Garnet is only present as a fractionated phase. Further garnet growth in the lower blueschist-facies field is then dependant on reaction kinetics that control element recycling from the fractionated garnet clasts back into the reacting bulk-rock composition. If all fractionated material remains in the garnet crystals produced so far, no new garnet grows until the rock reaches the blueschist- to eclogite-facies transition, as shown in Fig. 7f, which is calculated for the bulk-rock composition at the onset of the second garnet growth stage.

As mentioned above, interruptions during garnet growth might be characteristic for the shape of the P–T trajectory the sample followed during metamorphism. This correlation is evident in Fig. 6a and b, in which each of the six modelled zonation patterns is characterized by a characteristic compositional trend as well as the position and number of growth interruptions. For water-saturated conditions and garnet growth along path 1, two growth interruptions mark the three-stage garnet growth—a feature that is not observed in the natural sample (Fig. 6c). Also, the pattern calculated along path 3 does not resemble the measured profiles, because neither the increasing spessartine content nor the plateau-like almandine pattern in the core can be seen in the natural samples. In contrast, the pattern modelled along path 2 very closely resembles the measured one. The slight decrease in pyrope content associated with an increase in grossular content prior to the growth interruption can be observed in the natural sample. Also, the slight decrease in pyrope and XMg after the compositional break matches the natural pattern well. The growth interruption predicted by the model is also in agreement with the resorption structures and the intermediate spessartine increase observed at the core–rim transition in the natural samples, and indicated
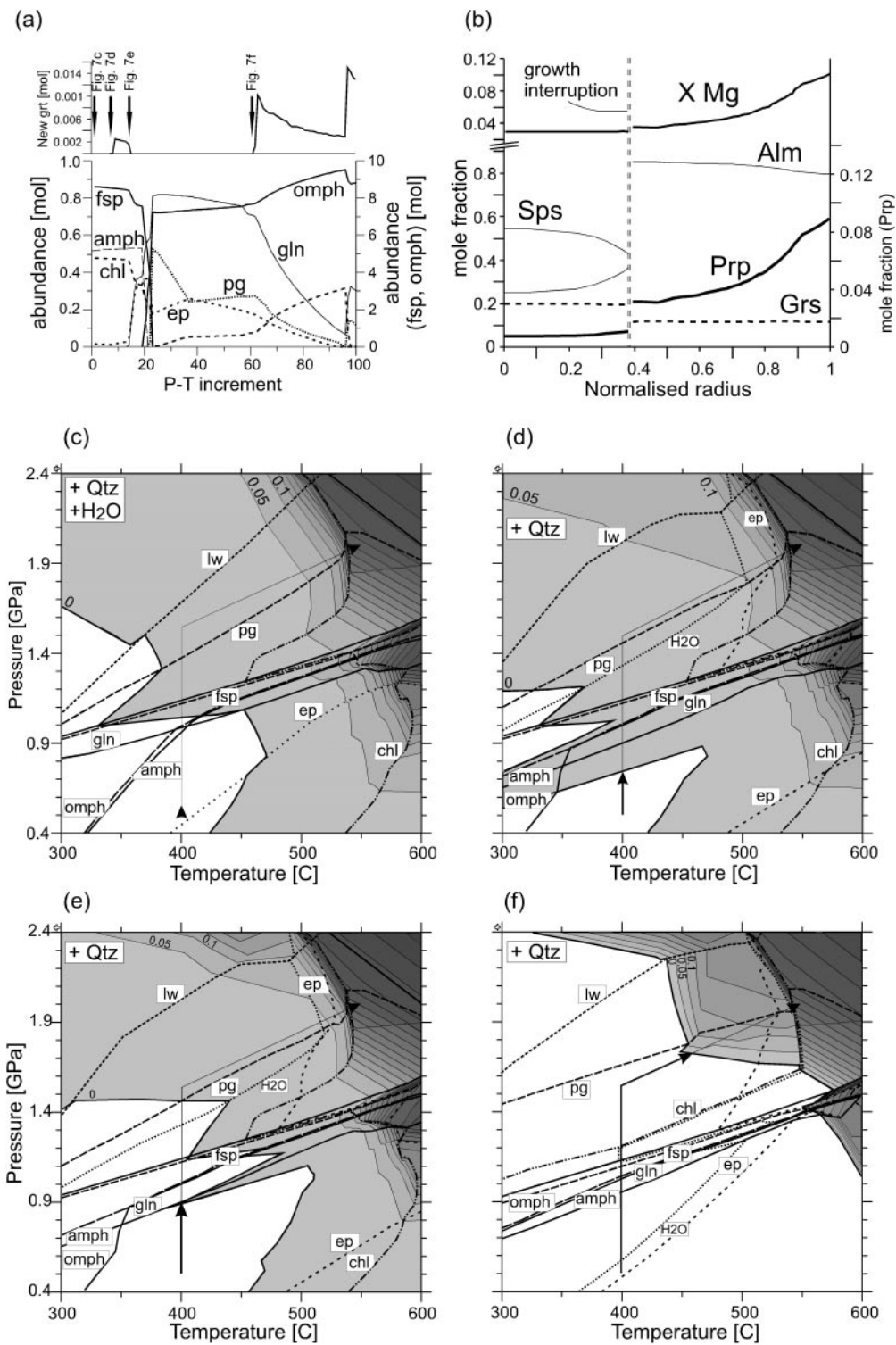
Fig. 7. Mineral abundance plot and *P–T* pseudosections showing the effect of fractional crystallization on garnet growth. (a) Garnet growth increment and modal abundance of garnet-influencing phases calculated along *P–T* path 3 for sample MK 35. The arrows in (a) mark the *P–T* increments for which the bulk composition is used to calculate the pseudosections (c)–(f). (b) Calculated core–rim garnet composition along path 3. (c)–(f) pseudosections and contours for molar abundance of garnet calculated for progressively depleted bulk-rock compositions according to the fractionation effects along path 3. Darker colours indicate higher values. Mineral labels are on the 'present' side. See Appendix for bulk-rock compositions and mineral abbreviations.
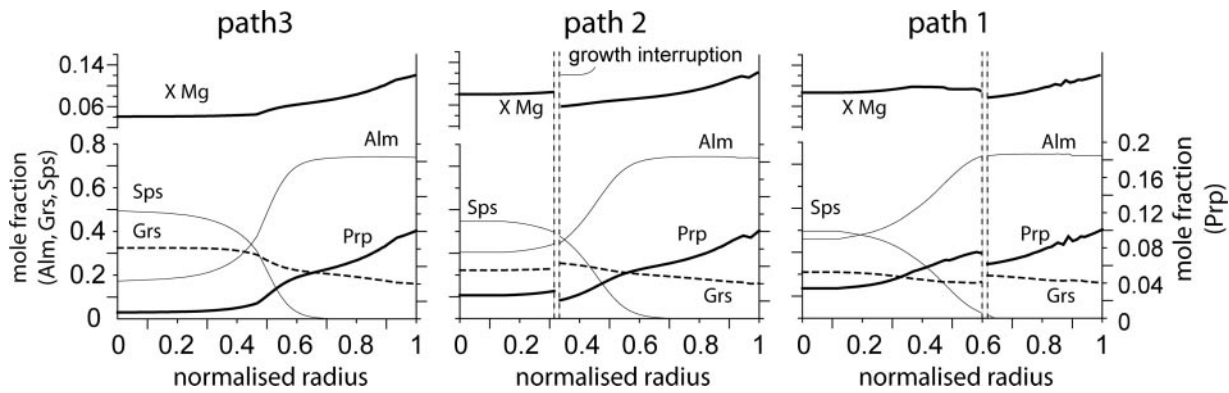
Fig. 8. Modelled garnet zonation patterns for sample MK 117 (groups II and III) for the different *P–T* trajectories assuming dehydration during metamorphism. None of the modelled patterns, which are very similar to those in Fig. 6, shows the same characteristics as the natural sample (cf. Fig. 4). Each profile is characterized by certain compositional changes and growth interruptions indicative of the sample's prograde *P–T* evolution.

by the resorbed cores of the atoll-like garnets in this sample (Fig. 3a). Interestingly, the pattern modelled along path 3 for the dehydration-only model (Fig. 6b) is in best agreement with the natural pattern, whereas those for paths 1 and 2 do not produce zonation patterns resembling those of the natural sample. Nevertheless, the comparison of modelled and observed garnet zonation patterns clearly indicates that garnet in sample MK 35 grew along a pressure-sensitive *P–T* trajectory rather than along a *P–T* path characterized by intense heating during compression. Further, the presence of a hydrous phase during metamorphism can be deduced from the modelled patterns.

MK 117 (group II garnets)

Figure 8 shows the modelled garnet zonation patterns along the three different paths for sample MK 117 and dehydration-only conditions. Starting with water-saturated conditions, the rock follows paths 1–3 undergoing fractional garnet crystallization and water fractionation, as in the previous models. It is obvious that none of the modelled zonation patterns in Fig. 8 resembles the compositional zonation of the group II garnets in sample MK 117. In all cases, initial garnet growth in the models starts with spessartine–grossular-rich compositions followed by a more or less smooth transition to almandine–pyrope-rich garnet rims. Neither the abrupt compositional break at the core-overgrowth transition nor the grossular-poor core displayed by the natural sample (Fig. 4c and d) can be observed in these model profiles. Thus, the complex zonation patterns of group II garnets must be of a different origin.

As mentioned above, the rocks of the Sesia Zone underwent pre-Alpine HT metamorphism with peak conditions around 750°C at 0·6–1·0 GPa. Thus, the possibility of preserving polymetamorphic garnet growth is evident. To reconstruct garnet growth in such a

polymetamorphic scenario, we modelled the growth for two different polymetamorphic *P–T* paths (not shown in Fig. 5): (1) along a prograde HT path from 400°C at 0·5 GPa to peak temperatures of 750°C at 0·8 GPa followed by HP path 3 for fractional crystallization and dehydration during metamorphism (Fig. 9a); (2) although several authors report pre-Alpine HT garnets with well preserved chemical zonation patterns, it is most likely that the growth zonation in these HT garnets equilibrated at amphibolite or granulite facies conditions, because volume diffusion in garnet becomes significantly faster at temperatures above 550°C. To account for that, we calculated the garnet zonation pattern with a core composition equilibrated at 750°C at 0·8 GPa, followed by Alpine overgrowth along path 3 (Fig. 9b).

In both cases, an almandine–pyrope-rich garnet is overgrown by an almandine-rich rim that shows a compositional trend towards more pyrope-rich composition at the outer rim. As in the profile in Fig. 9a, the first HP overgrowth shows slightly higher almandine contents than the garnet equilibrated at upper amphibolite facies. Both zonation patterns calculated for a polymetamorphic evolution show significant differences from those observed in the natural sample. Although the relative changes in grossular and pyrope contents are similar to those in the natural sample, the higher almandine content of the first overgrowth as well as the compositional trends in the HP overgrowth do not resemble those in the sample. Thus, other processes, discussed in the following paragraph, might be responsible for the complex compositional zonation patterns in group II garnets.

Apart from relict cores of metamorphic minerals, the pre-Alpine HT metamorphism might have influenced the initial water content of the Sesia rocks prior to the HP metamorphic overprint. Therefore, we modelled
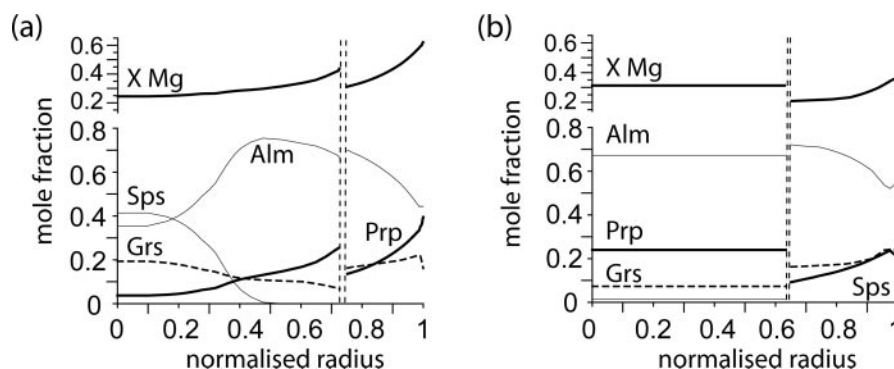
Fig. 9. (a) Modelled garnet zonation pattern assuming polymetamorphic garnet growth without diffusional equilibration. The internal part of the profile is the result of a prograde evolution up to upper amphibolite facies conditions (see text). The overgrowth after the growth interruption displays the HP garnet. (b) Modelled pattern assuming complete equilibration of the entire grain at upper amphibolite facies conditions (equilibrated core composition), followed by a HP evolution along path 2 (zoned rim).

garnet growth along the HP trajectory starting with different initial water contents. This calculation yielded interesting, quite unexpected results.

Figure 10 shows pseudosections, modelled mineral abundances and garnet zonation patterns calculated for sample MK 117 along path 3 for different initial water contents of the host-rock. The uppermost diagrams in Fig. 10 are calculated assuming water-saturated conditions, whereas the diagrams below are for increasing water-undersaturation. Water-undersaturation has a strong influence on the amount of garnet present at certain P–T conditions, on the initial garnet composition, as well as on the phase assemblage during metamorphic evolution. The pseudosections show that garnet growth starts at lower temperatures and that the amount of garnet is much higher in rocks with low water content than in water-saturated rocks. Due to mass balance constraints, garnet cores in water-undersaturated rocks have much lower spessartine contents. Interestingly, the grossular content is also extremely low in these garnets—a result of the different equilibrium mineral assemblage at greenschist-facies conditions for water-saturated and undersaturated conditions. For water-saturated conditions, initial garnet growth occurs mainly at the expense of chlorite, resulting in a spessartine–grossular-rich garnet. At water-undersaturated conditions, garnet growth starts in the presence of calcic amphibole and is mainly at the expense of biotite (Fig. 10) leading to almandine-rich, grossular-poor garnet cores. Thus, the difference in the equilibrium mineral assemblage caused by limited water-availability leads to significant changes in garnet composition and growth history.

The complex pattern in the rim overgrowth in the lowermost diagram in Fig. 10 is remarkable; this is a result of the short growth interruptions at the core–rim transition. The close-up BSE image in Fig. 4b shows the lighter garnet core with straight grain boundaries, which

are almost unaffected by resorption and overgrown by a small darker rim. The thickness of this overgrowth is highly variable and is marked by a thin light zone (arrow). The observed compositional profile across the rim of the natural sample (Fig. 4d) shows that the composition of the small dark zone differs significantly from the rest of the overgrowth. Almandine and pyrope show a characteristic minimum and grossular has an intermediate maximum in the small overgrowth zone. This complex chemical zonation as well as the two growth interruptions, which cause the complex zonation pattern in the garnet rim and might be responsible for the uneven distribution of rim material, can be predicted by assuming water-undersaturated conditions at initial garnet growth (lowermost diagrams in Fig. 10).

It is remarkable that despite higher modal amounts of garnet in the case of water-undersaturation of the host rock, fractional crystallization leads to growth interruptions during metamorphic evolution. The pseudosections in Fig. 11 demonstrate the P–T–X evolution of sample MK 117 assuming water-undersaturation (see Appendix Table 2 for calculated bulk rock compositions). Figure 11a, which is the same diagram as the lowermost pseudosection in Fig. 10, displays the phase relations for the initial bulk-rock composition. Garnet is stable in the entire grid and has high modal abundances, even at greenschist-facies conditions. Due to the high initial amount of garnet, fractional crystallization has a pronounced effect on the effective, i.e. reacting, bulk-rock composition. After a short period of garnet growth, depletion of the bulk-rock composition leads to a rapid decrease in garnet abundance in the entire grid (Fig. 11b). The diagram in Fig. 11c shows the enlarged P–T area marked by the rectangle in Fig. 11b and demonstrates how isothermal compression leads the sample into a phase field in which garnet is no longer part of the stable mineral assemblage. If no, or only a little, garnet is recycled into the effective bulk-rock
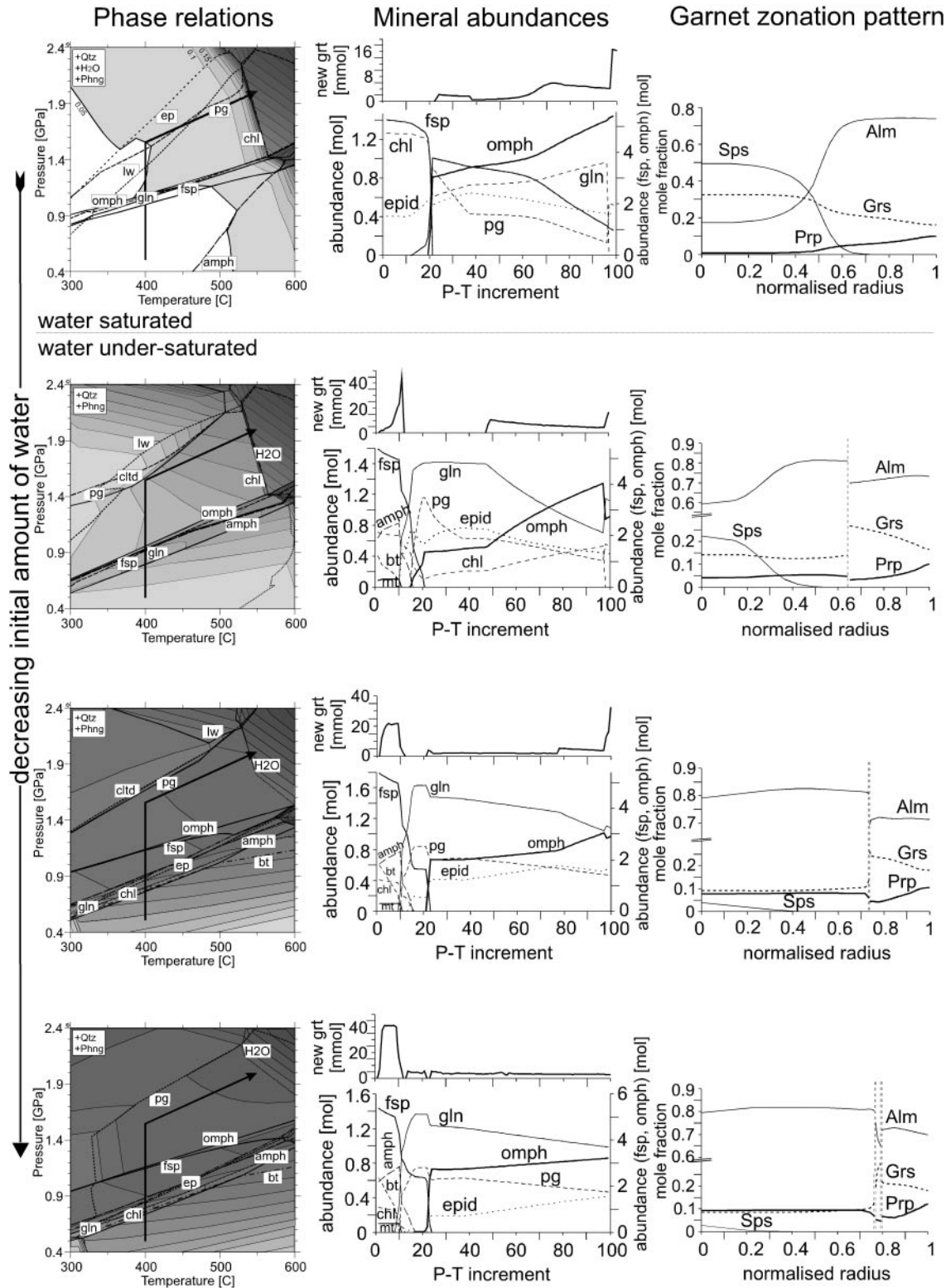
Fig. 10. Pseudosections for sample MK 117 with garnet molar isopleths (first column), garnet growth increments and mineral abundances (second column) and garnet zonation patterns (third column) calculated along path 3 with decreasing initial amount of water from top to bottom. The diagrams in the first row are calculated assuming water saturation (20 mol H_2O). The diagrams in subsequent rows are calculated with an initial water content of 6·25, 5 and 4·5 mol H_2O, respectively.
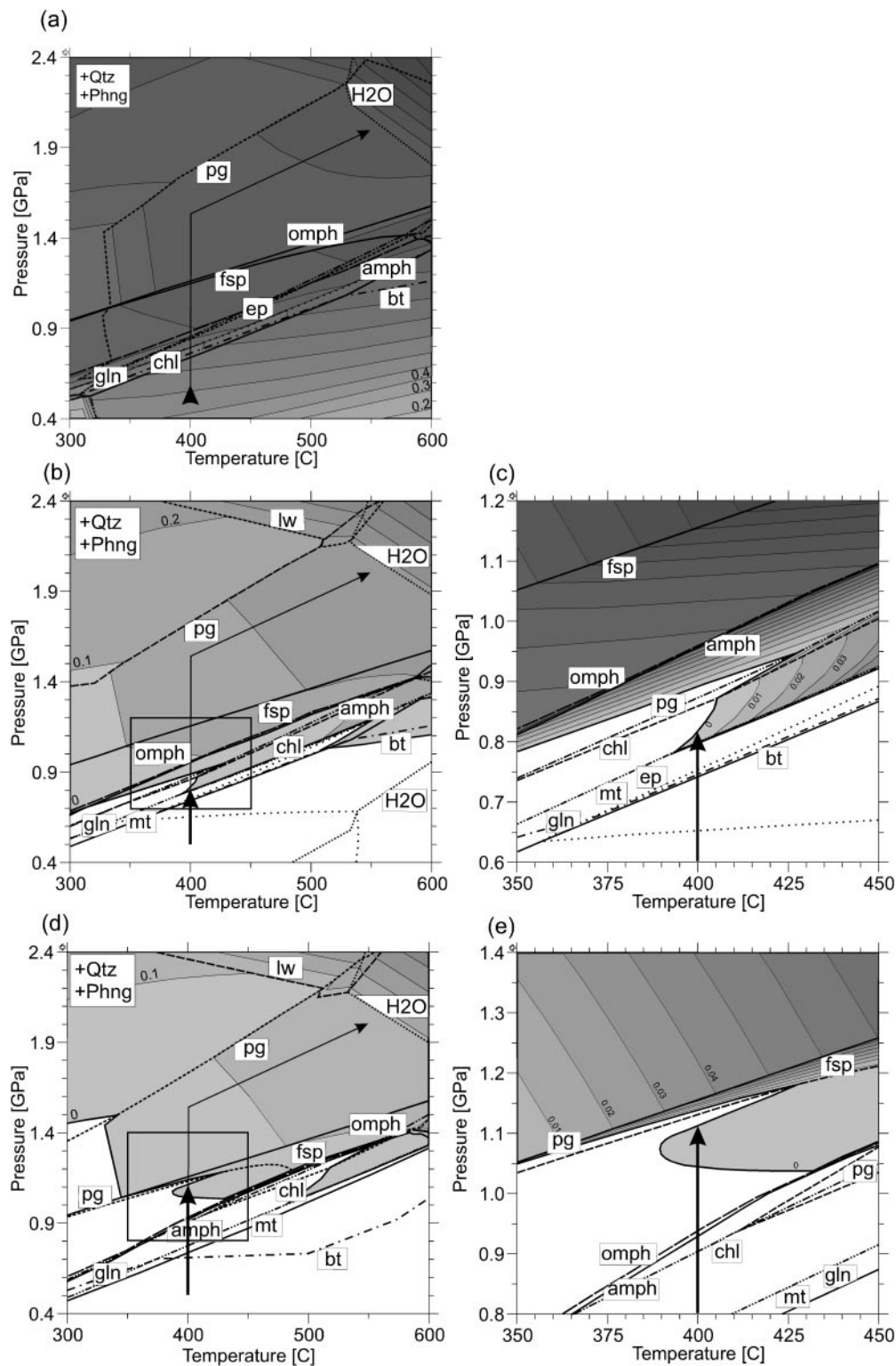
Fig. 11. Series of *P–T* pseudosections demonstrating the effect of fractional garnet crystallization in water-undersaturated rocks. (a) Pseudosection and garnet molar isopleths (shading) as shown in the bottom row in Fig. 10 calculated for the initial bulk-rock composition and water-undersaturated conditions. (b) and (c) Pseudosection and molar isopleths (shading) calculated for the depleted bulk-rock composition after the first garnet growth stage; the rectangle marks the enlargement shown in (c). (d) and (e) Pseudosection and molar isopleths (shading) calculated for the bulk-rock composition after the second garnet growth stage, the rectangle marks the enlargement in (e). Mineral labels are on the 'present' side.

Fig. 12. Comparison of natural and modelled zonation patterns of group III garnets. (a) Compositional core–rim profile across the group III garnet shown in Fig. 4f. (b) Calculated compositional profile modelled for garnet growth along path 3, but starting at 400°C and 0·8 GPa. The profile is calculated assuming water-undersaturation of the host rock and complete garnet resorption after the first growth stage.
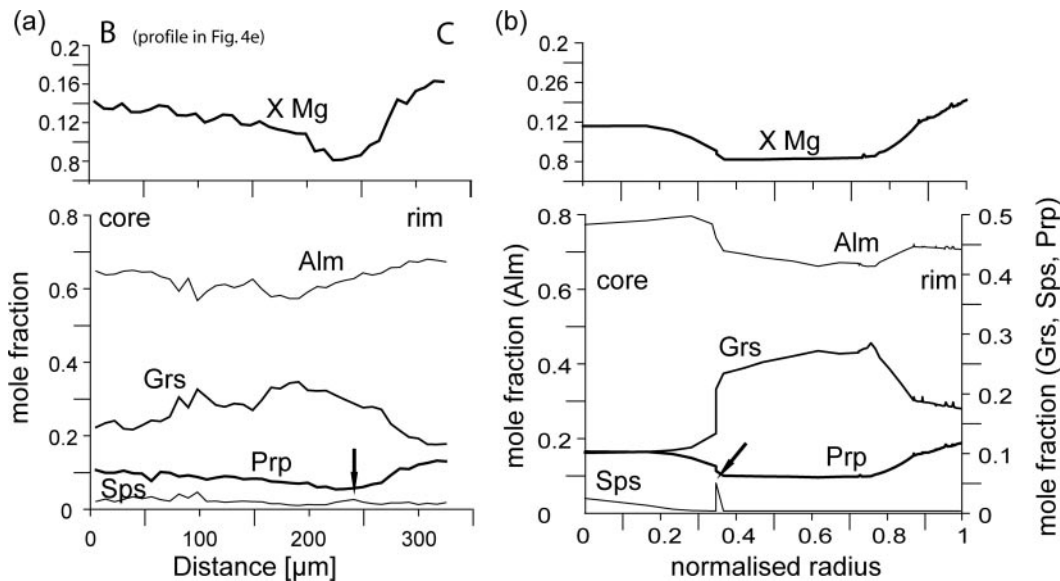
composition, garnet growth will be interrupted during compression between 0·8 and 0·9 GPa. The *P–T–X* relations after the second garnet growth stage are displayed in Fig. 11d and e. Due to the strongly curved zero mode line of garnet, the rock leaves the garnet stability field at about 1·1 GPa and the stable assemblage then consists of feldspar, sodic amphibole, omphacite, phengite, epidote and quartz (Fig. 11e).

MK 117 (group III garnets)
As mentioned above, garnets in this sample clearly show a bimodal size distribution, such that group III garnets have generally smaller grain sizes (0·1–0·5 mm) than group II garnets (1–5 mm). Thus, the question arises whether group III garnets in this sample grew later after the first or second growth interruption predicted by the thermodynamic forward model (Fig. 11). Although the growth interruptions predicted by the forward model only occur over a small *P–T* range (Fig. 11c and e), resorption might have affected at least parts of the fractionated garnet grains during the growth interruption. To test this possibility, we modelled garnet growth in this sample starting at 0·8 GPa and assuming that garnets grown during the first growth stage were completely resorbed.

Figure 12 shows a comparison between the core–rim profile (B–C in Fig. 4f) across the garnet shown in Fig. 4e and f (Fig. 12a) and the zonation pattern modelled along path 3 starting with the initial bulk-rock composition at 0·8 GPa (Fig. 12b). Although the absolute values of the garnet components are slightly different, especially in

the core, the relative change in the modelled profile resembles closely that from the natural sample. Both almandine and pyrope show a small plateau in the core followed by a slight decrease towards the inner rim and increasing values to the outer rim. As in the natural sample, grossular shows the opposite trend. Further, there is a slight increase in spessartine in the natural sample that coincides with the lowest pyrope content (arrow in Fig. 12a), possibly the result of decreasing garnet growth or garnet resorption. Although this increase occurs closer to the rim in the natural sample, the model also predicts an increase in spessartine at the core–rim transition (arrow in Fig. 12b). It is therefore very likely that there were three stages of garnet growth in this sample. Whereas group II garnets record all stages of garnet growth, group III garnets grew later in the metamorphic evolution and do not record the initial garnet growth stage in this sample. The fact that both group II and group III garnets occur in this sample may be due to the establishment of small-scale chemical domains, in turn leading to different effective bulk-rock compositions within the same sample.

DISCUSSION
P–T path information
The modelled garnet zonation patterns differ significantly for the three modelled *P–T* trajectories as well as for different water contents of the protolith. Thus, interpreting the shape of the *P–T* path in rocks with suspect water influx is not straightforward. For example, the pattern for group I garnets in sample MK 35

modelled by assuming water-saturated conditions along path 2 (Fig. 6a) is similar to the pattern modelled for dehydration only along path 3 (Fig. 6b). In both cases, pyrope and XMg rise steadily, except for a slight decrease along a small segment after the compositional break. This feature is also observed in the natural sample (Fig. 3c). In contrast to the pattern calculated for dehydration only, the patterns in the water-saturated models additionally show a rise in grossular content and a slight decrease in pyrope content prior to the compositional break. We take these features as evidence that the model conditions are similar to those during garnet growth in the natural sample, which implies that rocks containing group I garnets followed a pressure-sensitive, rather than a temperature-sensitive, P–T path under water-saturated or nearly water-saturated conditions. Although there is very little information about the prograde evolution of the Sesia rocks, the assumption of a fast, high dP/dT subduction path with a sufficient water supply is consistent with several publications that report pro- and also retrograde lawsonite formation in rocks from the southern part of the Mombarone Unit (Compagnoni et al., 1977; Pognante, 1989).

The importance of defining the P–T path is demonstrated in Fig. 13, which shows the calculated densities of rocks, the water content in hydrous minerals and the amounts of garnet and omphacite for P–T paths 1 and 3 at conditions of continuous dehydration. Additionally shown is the rocks' water content calculated for the water-saturated model. These plots clearly show that the densities differ significantly for pressures between 1·0 and 1·5 GPa, such that rocks following a pressure-sensitive path are much denser at the same depths than rocks following a more temperature-sensitive path. This difference is mainly due to the earlier formation of omphacite, as seen in Fig. 13a. The density difference is not observed between 1·5 and 1·8 GPa, where, in both cases, omphacite and quartz replace feldspar. Interestingly, rocks following path 3 show a significant increase in density between 1·7 and 2·0 GPa caused by intense garnet crystallization above 1·7 GPa.

The amount of water liberated by dehydration reactions is predicted to have a significant influence on the style of subduction, through its expected effect on fluid-induced melt production (e.g. Schmid and Poli, 1998) and rheology (e.g. Brocher et al., 2003; Zhang et al., 2004). Figure 13a shows that the dehydration of the subducted slab differs significantly for the different P–T trajectories. Whereas rocks following path 1 undergo intense dehydration between 0·5 and 0·9 GPa, the main water-liberating reactions in rocks along path 3 occur between 1·0 and 1·3 GPa. At the transition to the eclogite facies (above 1·8 GPa), all of the rocks undergo intense dehydration. Furthermore, it is notable that in the case of path 3, the dehydration of the subducted

slab as well as the main density changes due to phase transformations occur within the same narrow pressure range of 1·0–1·2 GPa. The coincidence between dehydration reactions and density changes, as displayed in Fig. 13b, might have significant influence on the rheological behaviour of the subducted slab and might facilitate earthquake generation and possibly enable large-scale tectonic processes such as slab break-off.

Figure 13a shows another important property of subducted rocks: water-saturated conditions in subducted rocks need intense water influx to maintain water saturation between 1·2 and 1·8 GPa. The curve labelled 'H$_2$O path 3, water saturated' clearly shows that rocks following path 3 are water-undersaturated between 0·5 and 1·0 GPa and between 1·2 and 1·9 GPa. This is important, because it indicates that water-saturated conditions in HP rocks can only be achieved by intense re-hydration and water addition during burial—a crucial implication for thermodynamic equilibrium calculations.

Water-undersaturation

The evolution of the fluid phase during subduction is a topic of heated discussion (Kerrick & Connolly, 1998; Schmidt & Poli, 1998; Kerrick & Connolly, 2001), because the fluids released by devolatilization reactions may cause subduction-related volcanism and may also be responsible for intermediate-depth earthquakes (e.g. Wiens, 2001; Tibi et al., 2003; Bock et al., 2000; Jung et al., 2004; Mishra & Zhao, 2004; Zhang et al., 2004). Alternatively, they may be recycled into the exosphere through the upper plate, which significantly contributes to Earth's fluid cycle. Moreover, the water content of the subducted slab partly determines the stable mineral parageneses and therefore partly controls the physical properties of the subducted material.

Our models for initial water-undersaturation of the subducted rocks show that garnet composition at lower P–T conditions is significantly different from in water-saturated rocks (Fig. 10). This difference results in an abrupt change in garnet composition at the transition between garnet cores and rims—a feature often observed in metamorphic garnets from different tectonic settings (e.g. O'Brien, 1997; Parkinson, 2000). Such zonation patterns are often interpreted as the result of poly-metamorphic garnet growth, unfortunately without absolute age constraints, because dating of small domains of garnet porphyroblasts is not a trivial task (e.g. Vance & O'Nions, 1990; Ducea et al., 2003; Thöni, 2002; Sölva et al., 2003; Thöni & Jagoutz, 1992), if not impossible in fine-grained samples. Additionally, incomplete isotopic equilibration and large analytical errors caused by mineral or fluid inclusions might lead to erroneous results (e.g. Luais et al., 2001). Our calculations show that complex zonation patterns with such
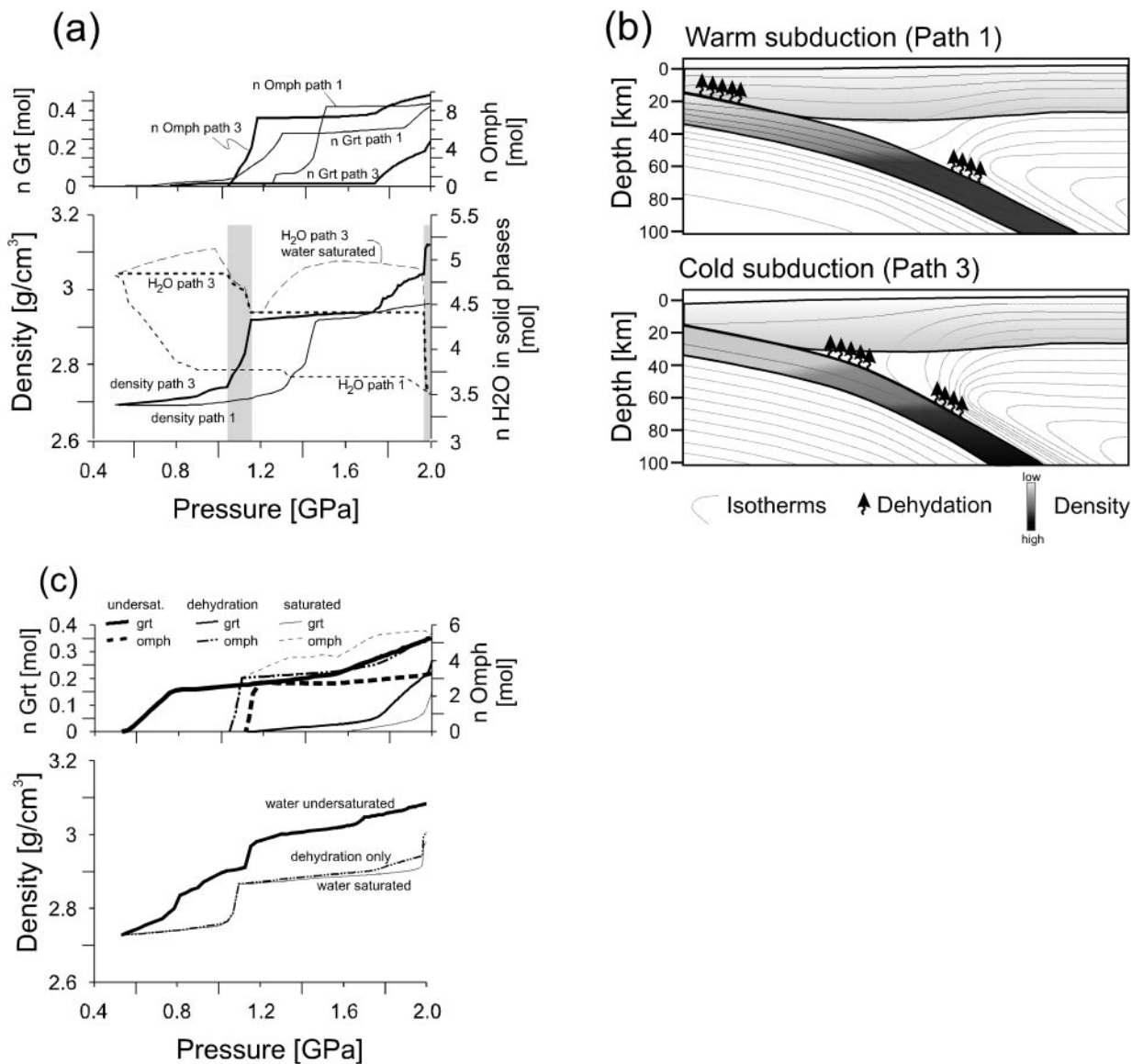
Fig. 13. The influence of water content and *P–T* paths on the physical properties of the subducted slab. (a) Molar garnet and omphacite abundance (upper diagram), densities (solid lines) and water content (dashed lines) of the subducted rocks (lower diagram) for contrasting *P–T* paths (paths 1 and 3). In the case of path 3, intense dehydration and density changes occur within small *P–T* intervals (shaded areas). In the case of path 1, dehydration and density changes coincide only at the transition to the eclogite facies. The thin dashed line shows H_2O content in water-saturated rocks. (b) Simplified models of warm and cold subduction zones displaying the depths of dehydration- and density-changing reactions depending on the *P–T* evolution of the subducted rocks. (c) Molar abundance of omphacite and garnet and density evolution in relation to the rock's initial water content. Note that water-undersaturated rocks become up to 10% denser than their water-saturated equivalents.

steep compositional gradients between core and rim compositions may result from the limited water content of the host rock prior to or during HP metamorphism. Apart from the tectonic implications, the interpretation of such chemical zonation patterns might yield insight into important mineral reactions as well as the fluid evolution in the subducted rocks.

The role of fluids during subduction has been investigated with stable isotopes, such as oxygen and hydrogen (e.g. Fu *et al.*, 2003; Nadeau *et al.*, 1993;

Yui *et al.*, 1995; Früh-Green *et al.*, 2001), as well as trace-element distribution in (U)HP rocks (e.g. Scambelluri & Philippot, 2001). Most recent publications show that the amount of free fluid, present during HP-metamorphism, is very limited or strongly channelized (Früh-Green, 1994) in most HP and UHP rocks, which has been inferred from a comparison of stable isotope ratios in (U)HP fluid inclusions with the ratios observed in the unmetamorphosed protoliths (e.g. Phillipot *et al.*, 1995; Zheng *et al.*, 1999; Cartwright & Barnicoat, 1999) as well
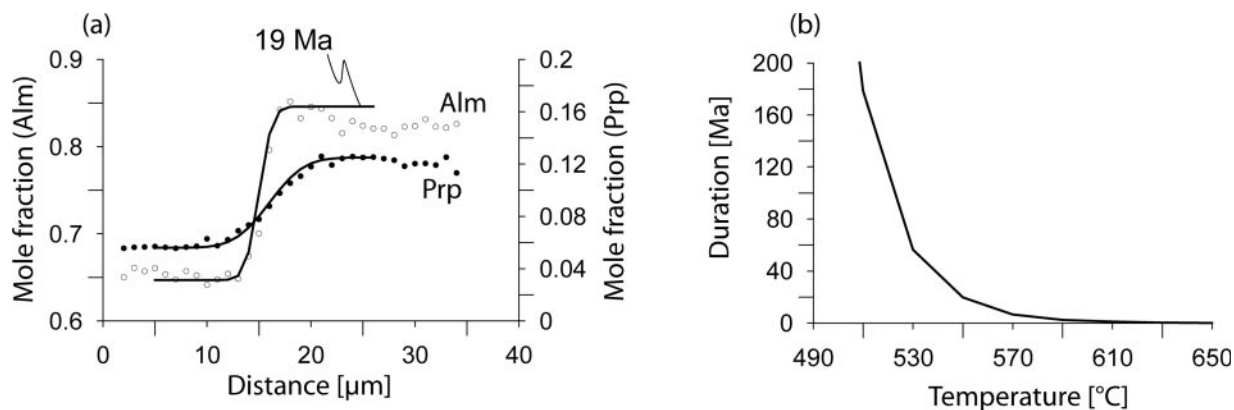
Fig. 14. Calculated diffusional relaxation of the step-like group II-zonation pattern observed in sample MK 117. The solid curve is calculated for 19 Myr of diffusional relaxation assuming peak temperatures of 550°C; the circles represent the measured compositional profile in the natural sample. (b) Calculated duration of metamorphism as a function of the peak temperature for the relaxation profile in (a).

as from the weak equilibration of trace elements between (U)HP minerals (e.g. Scambelluri & Philippot, 2001). Figure 13c shows that the density evolution of water-undersaturated rocks differs significantly from those metamorphosed with water present and those modelled for a dehydration-only scenario. Water-undersaturated rocks are up to 10% denser than the hydrated equivalents at blueschist-facies conditions, due to enhanced fractional garnet growth under water-undersaturated conditions.

Limited fluid availability also has significant influence on element transport mechanisms and therefore on chemical and isotopic equilibration in the entire rock, which in turn can lead to a misinterpretation of calculated phase equilibria and absolute age constraints, as shown in HP metamorphic rocks from the Eastern Alps (Thöni & Jagoutz, 1992). Fluids also seem to have been limited in the Sesia Zone, as indicated by a large scatter in the isotopic age constraints on peak metamorphism (Oberhänsli et al., 1985; Ruffet et al., 1997; Duchêne et al., 1997) and localized re-equilibration of pre-Alpine HT metamorphic mineral assemblages (Ridley, 1989; Stünitz, 1989).

Relaxation of the growth zonation due to volume diffusion

The interpretation of the garnet zonation patterns requires that the shape of the chemical zonation was established mainly during growth. Later modification of that pattern due to volume diffusion has been neglected in our calculations. Volume diffusion in garnet becomes important at temperatures above 550°C. The peak metamorphic conditions for the rocks considered in this study never exceeded 600°C (Reinsch, 1979; Desmons & O'Neil, 1978; Oberhänsli et al., 1985; Koons, 1986; Vuichard & Ballévre, 1988; Zucali et al., 2002), which minimizes the possibility of a significant modification of the growth zonation patterns in our samples. Because the

diffusional relaxation of chemical growth zonations contains information about the duration of metamorphic events, we calculated the effect of volume diffusion on a typical group II growth zonation pattern. We chose a zonation pattern with an abrupt change in composition in order to calculate the minimum time span of the metamorphic event. In Fig. 14a, the measured Fe- and Mg-profiles across the core–rim transition in sample MK 117 are shown. Also displayed are the profiles resulting from diffusional relaxation assuming an initial step-like growth zonation and 550°C peak temperatures. The profiles were calculated using the diffusion data from Chakraborty and Ganguly (1992) and an effective binary diffusion coefficient among the elements Fe, Mg, Ca and Mn. The profiles that display the best-fit curves to the measured zonation pattern are calculated for a duration of metamorphism of 19 Myr, which is in the range of commonly observed durations of metamorphic events. Because volume diffusion is strongly dependent on temperature, the calculated duration of metamorphism is a function of the peak metamorphic temperature. This dependence is shown in Fig. 14b. The calculations of the relaxation profiles show that diffusional modification due to volume diffusion does not significantly influence the growth zonation patterns, because the intrusion depth of volume diffusion in a garnet diffusion couple is less than 50 μm, whereas the compositional changes in the measured zonation patterns are much larger (e.g. Figs 3 and 4).

Regional implications

Previous authors have debated whether all units of the Sesia Zone had the same tectonometamorphic evolution during Alpine HP metamorphism (Ridley, 1989; Stünitz, 1989; Spalla et al., 1991). Though knowledge of the prograde evolution is essential for the investigation of processes responsible for the subduction of continental material to depths greater than 50 km, it is evident that,

compared with small continental fragments, a large coherent rock body will have much larger buoyant forces that hinder the burial of such terranes. In contrast, smaller slices of light continental material, if tectonically coupled to oceanic crust, can easily be subducted. Further, subduction will be facilitated by the density increase due to water-undersaturation of the continentally derived blocks. Our modelling indicates that large parts of the Mombarone nappe were not fully hydrated prior to Alpine HP metamorphism. In contrast, rocks belonging to the Bonze Unit, as well as in the vicinity of the nappe contacts, show evidence for water saturation prior to subduction. Difference in lithology and water content clearly indicates that the Sesia Zone consists of at least three different tectonic subunits that followed different P–T subduction paths. Subsequently, the water-saturated rocks of the Bonze Unit and the water-undersaturated rocks of the Mombarone Unit were folded during initial exhumation of the Mombarone Unit (cf. Ridley, 1989; Stünitz, 1989). This deformation obviously post-dated the regional distribution of garnet zonation patterns, which suggests that the Mombarone and Bonze Units were brought together on the retrograde path.

CONCLUSIONS

Three different types of garnet zonation patterns within the HP rocks of the Western Alpine Sesia Zone reflect different volatile conditions during pre-orogenic subduction and accretion of continental crust in the Western Alps. The regional correlation between garnet zonation patterns and sample locality confirms independent lithological and structural evidence that the Sesia Zone comprises units with different metamorphic histories during subduction.

The comparison of garnet zonation patterns derived from thermodynamic forward models that consider the effects of fractional crystallization and devolatilization during metamorphism with those observed in natural samples shows that these patterns are diagnostic of certain P–T paths and water content of the host rock during HP metamorphism. Group I garnets grew under water-saturated conditions, or close to water saturation, along a pressure-sensitive P–T path. Group II and III garnet zonation patterns reflect water-undersaturated conditions during prograde HP metamorphism. These models suggest that fluid migration was either restricted to localized channels or absent during the subduction of large segments of the Sesia Zone.

Water-undersaturation during subduction has a major influence on the physical properties of the subducted rocks. Due to enhanced garnet crystallization, the density of the subducted slab increases by up to 10% with respect to their water-saturated equivalents. Further, the shape of the prograde P–T trajectory reflects the interplay between dehydration reactions and density changes within the subducted slab. In case of a 'cool' (i.e. steep, pressure-sensitive) subduction path, dehydration reactions and the main density changes in the slab occur within a small P–T interval. For warm subduction, the depths of these phase transitions do not coincide. Our result show further that the method of thermodynamic forward modelling is an excellent tool to define more precisely P–T trajectories as well as the chemical evolution of the host rock during subduction processes.

SUPPLEMENTARY DATA

Supplementary data for this paper are available at *Journal of Petrology* online.

REFERENCES

Aoya, M., Uehara, S., Matsumoto, M., Wallis, S. R. & Enami, M. (2003). Subduction-stage pressure–temperature path of eclogite from the Sambagawa belt: prophetic record for oceanic-ridge subduction. *Geology* **31**, 1045–1048.

Arenas, R., Abati, J., Catalan, J. R. M., Garcia, F. D. & Pascual, F. J. R. (1997). P–T evolution of eclogites from the Agualada unit (Ordenes complex, northwest Iberian Massif, Spain): implications for crustal subduction. *Lithos* **40**, 221–242.

Avigad, D. (1996). Pre-collisional ductile extension in the internal Western Alps (Sesia Zone, Italy). *Earth and Planetary Science Letters* **137**, 175–188.

Ayres, M. & Vance, D. (1997). A comparative study of diffusion profiles in Himalayan and Dalradian garnets: constraints on diffusion data and the relative duration of the metamorphic events. *Contributions to Mineralogy and Petrology* **128**, 66–80.

Babist, J., Handy, M. R., Hammerschmidt, K. & Konrad-Schmolke, M. (in press). Multi-stage exhumation of high pressure rocks from a sliver of continental crust: an example from the Sesia zone, Italian Western Alps. *Tectonics*, in press.

Bock, G., Schurr, B. & Asch, G. (2000). High-resolution image of the oceanic Moho in the subducting Nazca plate from P–S converted waves. *Geophysical Research Letters* **27**, 3929–3932.

Brocher, T. M., Parsons, T., Trehu, A. M., Snelson, C. M. & Fisher, M. A. (2003). Seismic evidence for widespread serpentinized forearc upper mantle along the Cascadia margin. *Geology* **31**, 267–270.

Carraro, F., Dal Piaz, G. V. & Sacchi, R. (1970). Serie di Valpelline e II Zona Diorito-Kinzigitica sono i relitti di un ricoprimento proveniente dalla Zona Ivrea-Verbano. *Memorie della Società Geologica Italiana* **9**, 197–224.

Carswell, D. A. & Zhang, R. Y. (1999). Petrographic characteristics and metamorphic evolution of ultrahigh-pressure eclogites in plate-collision belts. *International Geology Review* **41**, 781–798.

Cartwright, I. & Barnicoat, A. C. (1999). Stable isotope geochemistry of Alpine ophiolites: a window to ocean-floor hydrothermal alteration and constraints on fluid-rock interaction during high-pressure metamorphism. *International Journal of Earth Sciences* **88**, 219–235.

Chakraborty, S. & Ganguly, J. (1992). Cation diffusion in alumino-silicate garnets; experimental determination in spessartine-almandine diffusion couples, evaluation of effective binary, diffusion coefficients, and applications. *Contributions to Mineralogy and Petrology* **111**, 74–86.

Chernoff, C. B. & Carlson, W. D. (1997). Disequilibrium for Ca during growth of pelitic garnet. *Journal of Metamorphic Geology* **15**, 421–438.

Compagnoni, R. & Hirajima, T. (2001). Superzoned garnets in the coesite-bearing Brossasco-Isasca Unit, Dora-Maira Massif, Western Alps, and the origin of the whiteschists. *Lithos* **57**, 219–236.

Compagnoni, R. & Maffeo, B. (1973). Jadeite-bearing metagranites l. s. and related rocks in the Mount Mucrone Area (Sesia-Lanzo Zone, Western Italian Alps). *Schweizerische Mineralogische und Petrographische Mitteilungen* **53**, 355–378.

Compagnoni, R., Dal Piaz, G. V., Hunziker, J. C., Gosso, G., Lombardo, B. & Williams, P. F. (1977). The Sesio-Lanzo Zone, a slice of continental crust with Alpine high pressure–low temperature assemblages in the western Italian Alps. *Rendiconti della Societa Italiana di Mineralogia e Petrologia* **33**, 335–374.

Connolly, J. A. D. (1995). Phase-diagram methods for graphitic rocks and application to the system C-O-H-FeO-TiO2-SiO2. *Contributions to Mineralogy and Petrology* **119**, 94–116.

Cooke, R. A., O'Brien, P. J. & Carswell, D. A. (2000). Garnet zoning and the identification of equilibrium mineral compositions in high-pressure–temperature granulites from the Moldanubian Zone, Austria. *Journal of Metamorphic Geology* **18**, 551–569.

Cygan, R. T. & Lasaga, A. C. (1982). Crystal-growth and the formation of chemical zoning in garnets. *Contributions to Mineralogy and Petrology* **79**, 187–200.

Dal Piaz, G. V., Gosso, G. & Martinotti, G. (1971). La II Zona Diorito-Kinzigitica tra la Valle Sesia e la Valle d'Ayas (Alpi Occidentali). *Memorie della Societa Geologica Italiana* **11**, 433–460.

Dal Piaz, G. V., Hunziker, J. C. & Martinotti, G. (1972). La Zona Sesia-Lanzo e l'evoluzione tettonico-metamorfica delle Alpi nordoc-cidentali interne. *Memorie della Societa Geologica Italiana* **11**, 433–466.

Dal Piaz, G. V., Hunziker, J. C. & Stern, W. B. (1978). The Sesia-Lanzo Zone, a slice of subducted continental crust? *US Geological Survey, Open File Report*, 83–86.

de Capitani, C. & Brown, T. H. (1987). The computation of chemical equilibrium in complex systems containing non-ideal solutions. *Geochimica et Cosmochimica Acta* **51**, 2639–2652.

Desmons, J. & O'Neil, J. R. (1978). Oxygen and hydrogen isotope compositions of eclogites and associated rocks from Eastern Sesia Zone (Western Alps, Italy). *Contributions to Mineralogy and Petrology* **67**, 79–85.

Ducea, M. N., Ganguly, J., Rosenberg, E. J., Patchett, P. J., Cheng, W. J. & Isachsen, C. (2003). Sm–Nd dating of spatially controlled domains of garnet single crystals: a new method of high-temperature thermochronology. *Earth and Planetary Science Letters* **213**, 31–42.

Duchêne, S., Blichert-Toft, J., Luais, B., Telouk, P., Lardeaux, J. M. & Albarede, F. (1997). The Lu–Hf dating of garnets and the ages of the Alpine high-pressure metamorphism. *Nature (London)* **387**, 586–589.

Enami, M. (1998). Pressure–temperature path of Sanbagawa prograde metamorphism deduced from grossular zoning of garnet. *Journal of Metamorphic Geology* **16**, 97–106.

Escuder-Viruete, J., Indares, A. & Arenas, R. (2000). *P–T* paths derived from garnet growth zoning in an extensional setting; an example from the Tormes gneiss dome (Iberian Massif, Spain). *Journal of Petrology* **41**, 78.

Früh-Green, G. L. (1994). Interdependence of deformation, fluid infiltration and reaction progress recorded in eclogitic metagranitoids (Sesia Zone, Western Alps). *Journal of Metamorphic Geology* **12**, 327–343.

Früh-Green, G. L., Scambelluri, M. & Vallis, F. (2001). O–H isotope ratios of high pressure ultramafic rocks: implications for fluid sources and mobility in the subducted hydrous mantle. *Contributions to Mineralogy and Petrology* **141**, 145–159.

Fu, B., Touret, J. L. R. & Zheng, Y. F. (2003). Remnants of premetamorphic fluid and oxygen isotopic signatures in eclogites and garnet clinopyroxenite from the Dabie-Sulu terranes, eastern China. *Journal of Metamorphic Geology* **21**, 561–578.

Ganguly, J. & Tirone, M. (1999). Diffusion closure temperature and age of a mineral with arbitrary extent of diffusion: theoretical formulation and applications. *Earth and Planetary Science Letters* **170**, 131–140.

Ganguly, Y., Chakraborty, S., Sharp, T. G. & Rumble, D. (1996). Constraint on the time scale of biotite-grade metamorphism during Acadian orogeny from a natural garnet–garnet diffusion couple. *American Mineralogist* **81**, 1208–1216.

Gosso, G. (1977). Metamorphic evolution and fold history in the eclogitic micaschists of the upper Gressoney Valley (Sesio-Lanzo Zone, Western Alps). *Rendiconti della Societa Italiana di Mineralogia e Petrologia* **33**, 389–407.

Holland, T.J.B. & Powell, R. (1998). An internally consistent thermodynamic data set for phases of petrological interest. *Journal of Metamorphic Geology* **16**, 309–343.

Hollister, L. S. (1966). Garnet zoning: an interpretation based on Rayleigh fractionation model. *Science* **154**, 1647–1651.

Jung, H., Green, H. W. & Dobrzhinetskaya, L. F. (2004). Intermediate-depth earthquake faulting by dehydration embrittlement with negative volume change. *Nature* **428**, 545–549.

Kerrick, D. M. & Connolly, J. A. D. (1998). Subduction of ophicarbonates and recycling of CO2 and H2O. *Geology* **26**, 375–378.

Kerrick, D. M. & Connolly, J. A. D. (2001). Metamorphic devolatil-ization of subducted marine sediments and the transport of volatiles into the Earth's mantle. *Nature* **411**, 293–296.

Konrad-Schmolke, M., Handy, M. R., Babist, J. & O'Brien, P. J. (2005). Thermodynamic modelling of diffusion-controlled garnet growth. *Contributions to Mineralogy and Petrology* **149**, 181–195.

Koons, P. O. (1986). Relative geobarometry from high-pressure rocks of quartzofeldspathic composition from the Sesia Zone, Western Alps, Italy. *Contributions to Mineralogy and Petrology* **93**, 322–334.

Lardeaux, J.-M. & Spalla, M. I. (1991). From granulites to eclogites in the Sesia Zone (Italian Western Alps): a record of the opening and closure of the Piedmont ocean. *Journal of Metamorphic Geology* **9**, 35–59.

Lardeaux, J.-M., Gosso, G., Kienast, J. R. & Lombardo, B. (1982). Metamorphism and deformation in Sesia-Lanzo Site (Western Alps). and eclogitization of Continental Crust. *Bulletin De La Societe Geologique De France* **24**, 793–800.

Lasaga, A. C. & Jiang, J. X. (1995). Thermal history of rocks: *P–T*-T paths from geospeedometry, petrological data, and inverse-theory techniques. *American Journal of Science* **295**, 697–741.

Lattard, D. (1975). Conditions de formation des roches appartenant au facies des schistes vert dans la zone de Sesia-Lanzo: Alpes Italiennes. *Comptes Rendus Hebdomadaires des Seances de l'Academie des Sciences, Serie D: Sciences Naturelles* **280**, 2629–2632.

Liou, J. G. & Zhang, R. Y. (1995). Significance of ultrahigh-*P* talc-bearing eclogitic assemblages. *Mineralogical Magazine* **59**, 93–102.

Liou, J. G., Hacker, B. R. & Zhang, R. Y. (2000). Geophysics: into the forbidden zone. *Science* **287**, 1215–1216.

Loomis, T. P. (1982). Numerical-simulation of the disequilibrium growth of garnet in chlorite-bearing aluminous pelitic rocks. *Canadian Mineralogist* **20**, 411–423.

Luais, B., Duchene, S. & de Sigoyer, J. (2001). Sm–Nd disequilibrium in high-pressure, low-temperature Himalayan and Alpine rocks. *Tectonophysics* **342**, 1–22.

Mäder, U. K. & Berman, R. G. (1992). Amphibole thermobarometry; a thermodynamic approach. *Current Research Part E - Geological Survey of Canada:* **92-1E**, 393–400.

Menard, T. & Spear, F. S. (1993). Metamorphism of calcic pelitic schists, Stratford Dome, Vermont: compositional zoning and reaction history. *Journal of Petrology* **34**, 977–1005.

Meyre, C., De Capitani, C. & Partzsch, J. H. (1997). A ternary solid solution model for omphacite and its application to geothermo-barometry of eclogites from the middle Adula Nappe (Central Alps, Switzerland). *Journal of Metamorphic Geology* **15**(6), 687–700.

Mishra, O. P. & Zhao, D. P. (2004). Seismic evidence for dehydration embrittlement of the subducting Pacific slab. *Geophysical Research Letters* **31**, L09610.

Nadeau, S., Philippot, P. & Pineau, F. (1993). Fluid inclusion and mineral isotopic compositions (H–C–O) in eclogitic rocks as tracers of local fluid migration during high-pressure metamorphism. *Earth and Planetary Science Letters* **114**, 431–448.

O'Brien, P. J. (1997). Garnet zoning and reaction textures in overprinted eclogites, Bohemian Massif, European Variscides: a record of their thermal history during exhumation. *Lithos* **41**, 119–133.

O'Brien, P. J. (1999). Asymmetric zoning profiles in garnet from HP–HT granulite and implications for volume and grain-boundary diffusion. *Mineralogical Magazine* **63**, 227–238.

Oberhänsli, R., Hunziker, J. C., Martinotti, G. & Stern, W. B. (1985). Geochemistry, geochronology and petrology of Monte Mucrone: an example of Eo-Alpine eclogitization of Permian granitoids in the Sesia–Lanzo Zone, Western Alps, Italy. *Chemical Geology* **52**, 165–184.

Okudaira, T. (1996). Temperature–time path for the low-pressure Ryoke metamorphism, Japan, based on chemical zoning in garnet. *Journal of Metamorphic Geology* **14**, 427–440.

Parkinson, C. D. (2000). Coesite inclusions and prograde compositional zonation of garnet in whiteschist of the HP–UHPM Kokchetav Massif, Kazakhstan: a record of progressive UHP metamorphism. *Lithos* **52**, 215–233.

Passchier, C. W., Urai, J. L., van Loon, J. & Williams, P. F. (1981). Structural geology of the central Sesia Lanzo Zone. *Geologie en Mijnbouw* **60**, 497–507.

Peacock, S. M. (1993). The importance of blueschist–eclogite dehydration reactions in subducting oceanic-crust. *Geological Society of America Bulletin* **105**, 684–694.

Peacock, S. M. & Wang, K. (1999). Seismic consequences of warm versus cool subduction metamorphism: examples from southwest and northeast Japan. *Science* **286**, 937–939.

Perchuk, A., Philippot, P., Erdmer, P. & Fialin, M. (1999). Rates of thermal equilibration at the onset of subduction deduced from diffusion modeling of eclogitic garnets, Yukon–Tanana Terrane, Canada. *Geology* **27**, 531–534.

Phillipot, P., Chevallier, P., Chopin, C. & Dubessy, J. (1995). Fluid composition and evolution in coesite-bearing rocks (Dora-Maira Massif, Western Alps): implications for element recycling during subduction. *Contributions to Mineralogy and Petrology* **121**, 29–44.

Pognante, U. (1989). Lawsonite, blueschist and eclogite formation in the southern Sesia zone (Western Alps, Italy). *European Journal of Mineralogy* **1**, 89–104.

Pognante, U., Talarico, F., Rastelli, N. & Ferrati, N. (1987). High pressure metamorphism in the nappes of the Valle dell'Orco traverse (Western Alps collisional belt). *Journal of Metamorphic Geology* **5**, 397–414.

Rebay, G. & Spalla, M. I. (2001). Emplacement at granulite facies conditions of the Sesia–Lanzo metagabbros: an early record of Permian riftig? *Lithos* **58**, 85–104.

Reddy, S. M., Wheeler, J. & Cliff, R. A. (1999). The geometry and timing of orogenic extension: an example from the Western Italian Alps. *Journal of Metamorphic Geology* **17**, 573–589.

Reinsch, D. (1979). Glaucophanites and eclogites from Val Chiusella, Sesia–Lanzo Zone (Italian Alps). *Contributions to Mineralogy and Petrology* **70**, 257–266.

Ridley, J. (1989). Structural and metamorphic history of a segment of the Sesia–Lanzo Zone, and its bearing on the kinematics of Alpine deformation in the Western Alps. *Geological Society of London, Special Publications* **45**, 189–201.

Rubatto, D., Gebauer, D. & Compagnoni, R. (1999). Dating of eclogite-facies zircons: the age of Alpine metamorphism in the Sesia–Lanzo Zone (Western Alps). *Earth and Planetary Science Letters* **167**, 141–158.

Ruffet, G., Gruau, G., Ballevre, M., Feraud, G. & Philippot, P. (1997). Rb–Sr and ^{40}Ar-^{39}Ar laser probe dating of high-pressure phengites from the Sesia Zone (Western Alps): underscoring of excess argon and new age constraints on the high-pressure metamorphism. *Chemical Geology* **141**, 1–18.

Scambelluri, M. & Phillipot, P. (2001). Deep fluids in subduction zones. *Lithos* **55**, 213–227.

Scambelluri, M., Müntener, O., Hermann, J., Piccardo, G. B. & Trommsdorff, V. (1995). Subduction of Water into the Mantle: history of an Alpine Peridotite. *Geology* **23**, 459–462.

Schmid, S. M., Zingg, A. & Handy, M. (1987). The kinematics of movements along the Insubric Line and the emplacement of the Ivrea Zone. *Tectonophysics* **135**, 47–66.

Schmid, S. M., Aebli, H. R., Heller, F. & Zingg, A. (1989). The role of the Periadriatic Line in the evolution of the Alps. In: Coward, M. P., Dietrich, D. & Park, R. G. (eds), *Alpine Tectonics. Geological Society, London, Special Publication*, **45**, 153–171.

Schmidt, M. W. & Poli, S. (1998). Experimentally based water budgets for dehydrating slabs and consequences for arc magma generation. *Earth and Planetary Science Letters* **163**, 361–379.

Sölva, H., Thöni, M. & Habler, G. (2003). Dating a single garnet crystal with very high Sm/Nd ratios (Campo basement unit, Eastern Alps). *European Journal of Mineralogy* **15**, 35–42.

Spalla, M. I., Lardeaux, J. M., Dal Piaz, G. V. & Gosso, G. (1991). Metamorphisme et tectonique a la marge de la Zone Sesia–Lanzo. *Memorie degli Instituti di Geologia e Mineralogia dell'Universita di Padova* **43**, 361–369.

Spear, F. S. (1988). Metamorphic fractional crystallization and internal metasomatism by diffusional homogenization of zoned garnets. *Contributions to Mineralogy and Petrology* **99**, 507–517.

Spear, F. S. (1988). The Gibbs Method and Duhem Theorem: the quantitative relationships among *P*, *T*, chemical-potential, phase-composition and reaction progress in igneous and metamorphic systems. *Contributions to Mineralogy and Petrology* **99**, 249–256.

Spear, F. S. & Daniel, C. G. (2001). Diffusion control of garnet growth, Harpswell Neck, Maine, USA. *Journal of Metamorphic Geology* **19**, 179–195.

Spear, F. S. & Menard, T. (1989). Program GIBBS: a generalized Gibbs method algorithm. *American Mineralogist* **74**, 942–943.

Spear, F. S. & Selverstone, J. (1983). Quantitative *P–T* path from zoned minerals: theory and tectonic applications. *Contributions to Mineralogy and Petrology* **83**, 348–357.

Spear, F. S., Kohn, M. J., Florence, F. & Menard, T. (1990). A model for garnet and plagioclase growth in pelitic schists: implications for thermobarometry and *P–T* path determinations. *Journal of Metamorphic Geology* **8**, 683–696.

Stünitz, H. (1989). Partitioning of metamorphism and deformation in the boundary region of the "Seconda Zona Diorito-Kinzigitica", Sesia Zone, Western Alps. PhD Dissertation, Zürich, Swiss Federal Institute of Technology: pp 244.

Thöni, M. (2002). Sm–Nd isotope systematics in garnet from different lithologies (Eastern Alps): age results, and an evaluation of potential problems for garnet Sm–Nd chronometry. *Chemical Geology* **185**, 255–281.

Thöni, M. & Jagoutz, E. (1992). Some new aspects of dating eclogites in orogenic belts: Sm–Nd, Rb–Sr, and Pb–Pb isotopic results from the Austroalpine Saualpe and Koralpe type-locality (Carinthia Styria, Southeastern Austria). *Geochimica et Cosmochimica Acta* **56**, 347–368.

Tibi, R., Bock, G. & Wiens, D. A. (2003). Source characteristics of large deep earthquakes: constraint on the faulting mechanism at great depths. *Journal of Geophysical Research-Solid Earth* **108**.

Tropper, P., Essene, E. J., Sharp, Z. D. & Hunziker, J. C. (1999). Application of K-feldspar–jadeite–quartz barometry to eclogite facies metagranites and metapelites in the Sesia Lanzo Zone (Western Alps, Italy). *Journal of Metamorphic Geology* **17**, 195–209.

Vance, D. & O'Nions, R. K. (1990). Isotopic chronometry of zoned garnets: growth kinetics and metamorphic histories. *Earth and Planetary Science Letters* **97**, 227–240.

Venturini, G. (1995). Geology, geochemistry and geochronology of the inner central Sesia Zone (Western Alps, Italy). *Memoires de Geologie Lausanne* **25**, 148.

Venturini, G., Martinotti, G., Armando, G., Barbero, M. & Hunziker, J. C. (1994). The Central Sesia–Lanzo Zone (Western Italian Alps): new field observations and lithostratigraphic subdivisions. *Schweizerische Mineralogische und Petrographische Mitteilungen* **74**, 111–121.

Vidal, O. & Parra, T. (2000). Exhumation paths of high-pressure metapelites obtained from local equilibria for chlorite-phengite assemblages. *Geological Journal* **35**, 139–161.

Vuichard, J. P. & Ballèvre, M. (1988). Garnet chloritoid equilibria in eclogitic pelitic rocks from the Sesia Zone (Western Alps): their bearing on phase-relations in high-pressure metapelites. *Journal of Metamorphic Geology* **6**, 135–157.

Walsh, E. O. & Hacker, B. R. (2004). The fate of subducted continental margins: two-stage exhumation of the high-pressure to ultrahigh-pressure Western Gneiss Region, Norway. *Journal of Metamorphic Geology* **22**, 671–687.

Wheeler, J. & Butler, R. W. H. (1993). Evidence for extension in the western Alpine Orogen: the contact between the oceanic Piemonte and overlying continental Sesia units. *Earth and Planetary Science Letters* **117**, 457–474.

Wiens, D. A. (2001). Seismological constraints on the mechanism of deep earthquakes: temperature dependence of deep earthquake source properties. *Physics of the Earth and Planetary Interiors* **127**, 145–163.

Williams, P. F. & Compagnoni, R. (1983). Deformation and metamorphism in the Bard area of the Sesia Lanzo Zone, Western Alps, during subduction and uplift. *Journal of Metamorphic Geology* **1**, 117–140.

Yui, T. F., Rumble, D. & Lo, C. H. (1995). Unusually low Delta-O-18 ultra-high-pressure metamorphic rocks from the Sulu Terrain, Eastern China. *Geochimica et Cosmochimica Acta* **59**, 2859–2864.

Zhang, J. F., Green, H. W., Bozhilov, K. & Jin, Z. M. (2004). Faulting induced by precipitation of water at grain boundaries in hot subducting oceanic crust. *Nature* **428**, 633–636.

Zhang, R. Y., Liou, J. G., Ernst, W. G., Coleman, R. G., Sobolev, N. V. & Shatsky, V. S. (1997). Metamorphic evolution of diamond-bearing and associated rocks from the Kokchetav Massif, northern Kazakhstan. *Journal of Metamorphic Geology* **15**, 479–496.

Zheng, Y. F., Fu, B., Xiao, Y. L., Li, Y. L. & Gong, B. (1999). Hydrogen and oxygen isotope evidence for fluid–rock interactions in the stages of pre- and post-UHP metamorphism in the Dabie Mountains. *Lithos* **46**, 677–693.

Zucali, M., Spalla, M. I. & Gosso, G. (2002). Strain partitioning and fabric evolution as a correlation tool: the example of the Eclogitic Micaschists Complex in the Sesia–Lanzo Zone (Monte Mucrone–Monte Mars, Western Alps, Italy). *Schweizerische Mineralogische und Petrographische Mitteilungen* **82**, 429–454.

APPENDIX

Analytical procedure
Bulk-rock chemistry

Bulk-rock chemistry was determined by XRF analysis of hand specimen-sized samples using a SIEMENS SRS 3000 wavelength-dispersive XRF spectrometer at the Museum of Natural History of the Humboldt University Berlin. All analyses were made on fused glass discs prepared from dried and ignited powdered samples.

Mineral abbreviations

Amph = calcic amphibole, bt = biotite, chl = chlorite, cltd = chloritoid, ep = epidote, fsp = feldspar, gln = sodic amphibole, lw = lawsonite, mt = magnetite, omph = omphacite, pg = paragonite, phng = phengitic white mica, qtz = quartz.

Electron microprobe analysis

Microprobe analyses were carried out at the Museum of Natural History of the Humboldt University, Berlin, with a JEOL 8800 Superprobe, equipped with four wavelength-dispersive spectrometers. Measurement conditions were 15 kV acceleration voltage and a beam current of 15 nA. Beam diameter was 1 μm. For calibration, we used natural standard materials and for post-analytical correction, we used the ZAF algorithm.

Thermodynamic calculation routine

The algorithm of THERIAK calculates the stable mineral assemblage by minimizing the Gibbs free energy (G) in a multicomponent system with fixed bulk-rock composition. These calculations involve several steps including linear and non-linear programming problems. In the first step, THERIAK searches each solution phase for the composition with the lowest Gibbs energy of formation ($\Delta_f G$) in the system. The solid solution phases are defined by endmembers, i.e. each solution is considered to be made

Table 1: Bulk-rock composition of the samples used in the forward calculations

wt % oxide			Moles element			Mol % element		
Element	MK 117	MK35	Element	MK 117	MK 35	Element	MK 117	MK 35
SiO$_2$	68·40	69·50	Si	66·23	65·94	Si	24·50	24·55
TiO$_2$	0·78	0·52	Ti	n.c.*	n.c.	Ti	n.c.	n.c.
Al$_2$O$_3$	13·90	14·70	Al	15·86	16·44	Al	5·87	6·12
FeO	5·57	3·66	Fe	4·51	2·90	Fe	1·67	1·08
MnO	0·07	0·05	Mn	0·06	0·04	Mn	0·02	0·02
MgO	2·48	1·39	Mg	3·58	1·97	Mg	1·32	0·73
CaO	1·92	1·38	Ca	1·99	1·40	Ca	0·74	0·52
Na$_2$O	2·67	4·53	Na	5·01	8·33	Na	1·85	3·10
K$_2$O	2·23	2·46	K	2·75	2·98	K	1·01	1·11
LOI	1·70	1·10	varying amounts of H$_2$O added in the calculations (see text)					
			O	170·38	168·60	O	63·02	62·77
Sum	99·72	99·29	Sum	270·38	268·60			

* n.c., not considered.

Table 2: Rock compositions used for the pseudosection calculations in Figs 7 and 11

	Rock compositions Fig. 7 (moles)				Rock compositions Fig. 11 (moles)			
Element	Fig. 7c	Fig. 7d	Fig. 7e	Fig. 7f	Element	Fig. 11a	Fig. 11b	Fig. 11d
Si	65·94	65·94	65·90	65·87	Si	66·23	63·29	62·99
Al	16·44	16·44	16·41	16·39	Al	15·86	13·90	13·70
Fe	2·90	2·90	2·89	2·88	Fe	4·51	2·16	1·95
Mn	0·04	0·04	0·02	–	Mn	0·06	–	–
Mg	1·97	1·97	1·97	1·96	Mg	3·58	3·32	3·31
Ca	1·40	1·40	1·39	1·39	Ca	1·99	1·72	1·64
Na	8·33	8·33	8·33	8·33	Na	5·01	5·01	5·01
K	2·98	2·98	2·98	2·98	K	2·75	2·75	2·75
O	188·60	173·45	173·28	172·73	O	174·88	163·12	161·90
H	40	9·69	9·69	8·83	H	9·0	9·0	9·0

of any number of species, where each of these species is a valid end-member. $\Delta_f G$ of the solid solutions is defined by the Gibbs-Duhem equation:

$$\Delta_f G = \sum_{j=1}^{ne} x_j \cdot \mu_j,$$

where ne = number of endmembers in the solution phase, μ_j = chemical potential of end-member j in the solution phase, x_j = concentration of end-member j in the solution phase and $\mu_j = \mu_j^0 + \alpha \cdot R \cdot T \cdot \ln(a_j)$, where μ_j^0 = chemical potential of pure end-member j, α = site occupancy integer, R = Gas constant, T = temperature and a_j = activity of component j in the solution phase.

The solid solution models and Margules parameters used to determine $\Delta_f G$ are given below. The compositions with the smallest $\Delta_f G$ are added to the database as phases with fixed composition.

In the second step, THERIAK determines the mineral assemblage with the lowest Gibbs free energy. This problem can be formulated as:

$$\text{minimize } G = \sum_{k=1}^{N} n_k \cdot g_k,$$

where n_k is the number of moles, g_k is the molar Gibbs free energy of phase k and N is the number of coexisting phases in the system. Details of the algorithm are described in de Capitani and Brown (1987).

Solid solution models used in the forward calculations

Garnet

End-members: Pyrope, Grossular, Almandine, Spessartine.

Ideal one-site-mixing and Margules-type excess function.

Solid solution model: Ganguly *et al.* (1996).

Clinopyroxene

End-members: diopside, hedenbergite, jadeite.
One-site-mixing and Margules-type excess function.
Solid solution model: Meyre *et al.* (1997).

Sodic amphibole

End-members: Glaucophane, Fe-glaucophane.
One-site-mixing and Margules-type excess function:

	W^H	W^S	W^V
Glaucophane–Fe-glaucophane			
112	10 000	0·00	0·00

Phengite

End-members: muscovite, celadonite, Fe-celadonite, pyrophyllite.

One-site-mixing and Margules-type excess function:

	W^H	W^S	W^V
Muscovite–celadonite			
112	−10 500·0	55·0	0·79
Muscovite–Fe-celadonite			
112	−10 500·0	15·0	0·78
Muscovite–pyrophyllite			
112	30 000·0	20·0	−0·17
122	30 000·0	20·0	−0·17

Modified from Vidal and Parra (2000).

Chlorite

End-members: amesite, clinochlore, daphnite, Mn-chlorite.

Three-site-mixing and Margules-type excess function:

	W^H	W^S	W^V
Amesite–clinochlore			
112	−9400	−30	−0·2
Amesite–daphnite			
112	−12 000	35	0·5
Mn-chlorite–daphnite			
112	−10 000	0	0

Modified from Vidal and Parra (2000).

Calcic amphibole

End-members: pargasite, Fe-pargasite, tremolite, tschermakite, Fe-tschermakite, ferro-actinolite

Three-site-mixing and Margules-type excess function:

	W^H	W^S	W^V
Pargasite–tremolite			
112	9743·68	0	0
Tremolite–ferro-actinolite			
112	2108·23	0	0
Tschermakite–tremolite			
112	21 431·32	0	0
Fe-tschermakite–ferro-actinolite			
112	−15 492·29	0	0
Tschermakite–Fe-tschermakite			
112	2108·23	0	0
Pargasite–Fe-pargasite			
112	2108·23	0	0

Modified from Mäder and Berman (1992).

Biotite

End-members: phlogopite, eastonite, annite, ordered biotite

Three-site-mixing and Margules-type excess function:

	W^H	W^S	W^V
Phlogopite–annite			
112	9000·0	0	0
Phlogopite–eastonite			
112	10 000	0	0
Phlogopite–O-biotite			
112	3000	0	0
Annite–eastonite			
112	−1000	0	0
Annite–O-biotite			
112	6000	0	0
Eastonite–O-biotite			
112	10 000	0	0

Feldspar

End-members: albite, anorthite, K-feldspar
One-site-mixing and Margules-type excess function.
Solid solution model: Furman and Lindsley (1988).